RICE UNIVERSITY

Second-Harmonic Generation for Narrow-Line Cooling of ^{7}Li

by

De Luo

A Thesis Submitted
in Partial Fulfillment of the
Requirements for the Degree

Master of Science

Approved, Thesis Committee:

Randall G. Hulet, Chair
Fayez Sarofim Professor of Physics and Astronomy

Thomas C. Killian,
Professor of Physics and Astronomy

Kevin Kelly
Associate Professor of Electrical and Computer Engineering

Houston, Texas

January, 2017

Contents

List of Figures

1 Introduction

Bose-Einstein condensation (BEC) is a state of matter of a dilute Boson gas cooled to a temperature close to absolute zero. A large fraction of particles occupy the quantum state with the lowest energy, leading to a macroscopic quantum phenomenon. BEC provides an ideal testing ground for a wide range of problems in fundamental physics, such as matter-wave solitons [1, 2], Efimov few-body physics [3], and quantum vortices [4]. Proposed in 1924 by Bose and Einstein, it was first experimentally observed in 1995 with neutral atoms [5–7]. The transition temperature in a typical experiment is less than 1 μK, whereas the initial temperature is on the order of 10^3 K. To overcome the challenge of cooling the atomic gas over many orders of magnitude, many techniques such as laser cooling and evaporative cooling have been invented [8].

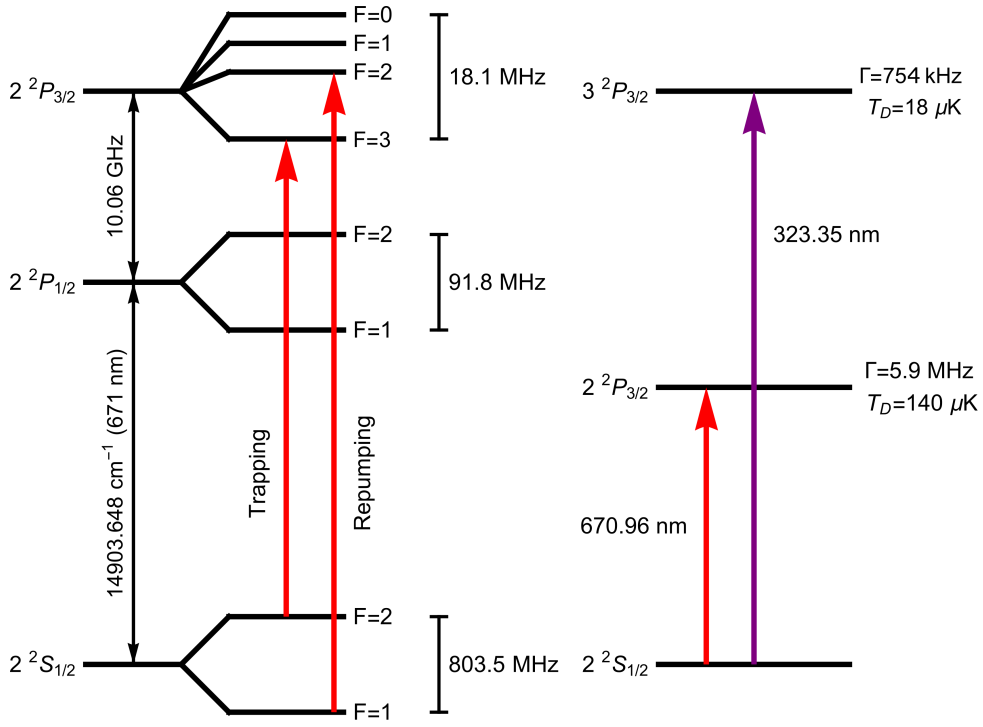

Figure 1: Energy levels of ^{7}Li. **a.** Laser cooling at 671 nm uses the cycling transition 2 $^2S_{1/2}$ to 2 $^2P_{3/2}$. **b.** Compared to the transition to 2 $^2P_{3/2}$, the transition to 3 $^2P_{3/2}$ at 323 nm has a lower Doppler temperature due to its narrower linewidth. The data is acquired from Ref. [19] and Ref. [20].

Our lab has an experimental apparatus (EMT2) that produces BECs of ^{7}Li atoms. A simplified energy level diagram highlighting the trapping and repumping transitions is shown in Fig. 1 (a). We use the 2 $^2S_{1/2}$ to 2 $^2P_{3/2}$ transition at 671 nm. Fig. 2 displays a schematic

of the apparatus. Lithium atoms are heated to approximately 500°C in an oven to produce a collimated atomic beam. The first stage of cooling is the Zeeman slower [9]. Photons from a near-resonant, counter-propagating laser beam are absorbed by the atoms. This causes the atoms to slow down, due to momentum conservation. The atoms in the excited state will spontaneously emit photons in random directions, making no change to the atom velocity, on average. A spatially-varying magnetic field tunes the transition energy by the Zeeman effect, such that the Doppler shifted frequency of the laser beam stays in resonance with the decelerating atoms. The atoms are cooled to about 1 mK by the Zeeman slower. Then the atoms pass through a 2-dimensional magneto-optical trap (2D MOT), which limits the spread of the atomic beam in the radial direction. In the center of the chamber, a 3D MOT, consisting of six laser beams, traps and cools the atoms. The temperature in the MOT is limited by the natural linewidth of the transition,

$$T_{\mathrm{D}} = \frac{\hbar\Gamma}{2k_B} \tag{1}$$

where the linewidth $\Gamma = 2\pi \times 5.9$ MHz and $T_{\mathrm{D}} = 140\ \mu$K [20]. In practice, at the end of our MOT stage the temperature is about 600 μK with 10^9 atoms. The next stage of cooling happens in a magnetic trap [10]. Atoms are pumped into the $|F = 2, m = 2\rangle$ state. This state is low-field seeking, so they can be trapped in the bottom of a 3-dimensional magnetic curvature. Radio-frequency (RF) radiation can selectively transfer atoms with higher energy to the $|F = 1, m = 1\rangle$ state. This state is high-field seeking, so the atoms are ejected from the trap. The remaining atoms rethermalize, reducing the average temperature. This process is repeated while the RF frequency is ramped to eject atoms with lower and lower energy. At the end of this forced evaporation we have a sample of 10^7 atoms at 20 μK. Then, the atoms are transfered into an optical dipole trap (ODT) [11] formed by a far-detuned (1070 nm), focused laser beam. The optical power in the laser beam is reduced gradually from 1 W to 30 mW, reducing the trap depth and allowing hot atoms to leave the trap. After this second stage of evaporation, the atom cloud contains about $8{\times}10^5$ atoms at 0.1 μK, and a BEC is formed with a condensate fraction above 90%.

While the system has worked well for more than a decade, we are looking for ways to simplify the cooling procedure. In some cases, sub-Doppler cooling can be achieved, resulting in a

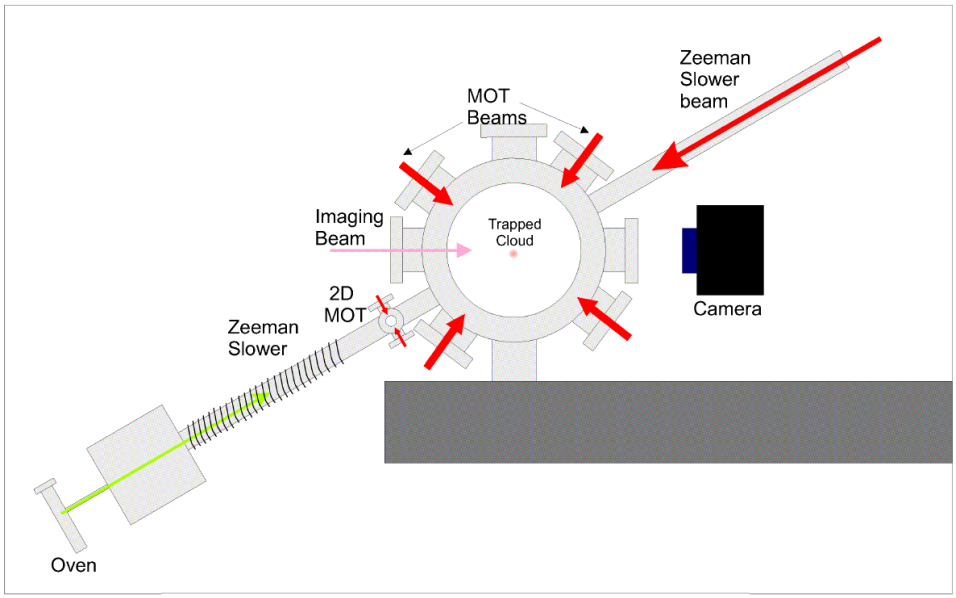

Figure 2: Schematic of the BEC experiment. This figure is reproduced from Ref. [12].

lower temperature limit, given by the recoil energy $T_R = \frac{\hbar^2 k^2}{2mk_B}$. One such technique is Sisyphus cooling [13]. The technique works for atom species like sodium [14], whose energy separation in the excited state hyperfine levels are large compared to the transition linewidth. This is not the case for the lithium $2\ ^2S_{1/2}$ to $2\ ^2P_{3/2}$ transition, so originally it was thought that the method cannot be applied to lithium. However, in a recent experiment, Sisyphus cooling with ^{7}Li atoms is realized, with a temperature of 40 μK in one dimension and 100 μK in three dimensions [15]. Another experiment combines the gray molasses technique and velocity-selective coherent-population trapping technique, using the ^{7}Li D1 ($2\ ^2S_{1/2}$ to $2\ ^2S_{1/2}$) transition, to achieve a temperature of 60 μK after the regular MOT cooling stage [16]. This method requires a separate laser system that produces about 150 mW light at 671 nm.

Another option is a direct transfer between the MOT and ODT, thus bypassing the magnetic trap stage. While this is entirely possible, and has been realized in some experiments [17], a constraining factor is the laser power required for the ODT to capture the sample at a relatively high temperature. To facilitate a direct transfer, we plan on reducing the initial temperature by using the $2\ ^2S_{1/2}$ to $3\ ^2P_{3/2}$ transition in ^{7}Li. As shown in Fig. 1 (b), this transition has a much narrower linewidth, 754 kHz [18], which corresponds to a T_D of 18 μK. APP3, a fermion experiment in our lab, has successfully used this narrow-line cooling method to achieve an all-optical production of a degenerate Fermi gas of ^{6}Li [21]. In their experiment, a commercial

frequency-doubling system (Toptica TA/DL-SHG 110) is used to generate the 323 nm light for laser cooling. The atoms are initially cooled by a red 671 nm MOT, then transferred to the UV MOT where it reaches a temperature of 50 μK. At this point, a direct transfer to an optical dipole trap can be achieved with moderate ODT power. In addition, it is possible to continue laser cooling in the ODT if the differential ac-Stark shift produced by the ODT light for the $2S_{1/2}$ and $3P_{3/2}$ is sufficiently small. Our ODT operates at 1070 nm, which is a "magic wavelength" where the polarizability of these states are identical [22]. Thus the differential light shift vanishes, and the atoms can be laser cooled in the ODT to very high phase-space densities [21].

We plan to implement the same cooling method. Our experiment can benefit from this upgrade for two reasons. First, we can eliminate the magnetic trapping stage, reducing the level of required maintenance. Second, the experiment cycle time can be reduced significantly.

Unfortunately, generating enough laser power at 323 nm is less straightforward than at 671 nm. Thus, commercially available lasers operate in the UV range are typically expensive. APP3 uses a frequency-doubling system designed by Toptica. It contains a diode laser that generates 646 nm light, a tapered amplifier that amplifies the diode output, and a frequency doubling cavity that uses a nonlinear crystal to generate 323 nm light. The system is capable of producing 60 mW of UV light. In another experiment, Wilson et al. have used a sum-frequency generation (SFG) of two NKT fiber lasers at 1051 nm and 1550 nm to generate 626 nm light, and frequency double to 313 nm [24]. For the SFG, 5 W at each wavelength is combined in a periodically-poled lithium niobate (PPLN) crystal to produce 2 W at 626 nm. The frequency doubler then produces 750 mW at 313 nm. This approach can be adapted to generate 323 nm, as reported in Ref. [25]. In comparison, although the SFG approach can produce much more UV power (10×), the fiber lasers cost much more than the diode laser and tapered amplifier. Common to both approach is a frequency doubling cavity. We have decided to first build a system based on the Toptica design. The frequency doubler can be used if in the future we adopt SFG approach for more power.

This thesis is organized as follows. In Chapter 2, we begin with a discussion of the principles of second-harmonic generation, and go through the design procedure of our doubling cavity. A detailed description of the laser system is followed by a report of its current status. For future reference, we also discuss the option of using fiber lasers and sum-frequency gen-

eration to produce light at 646 nm. In the following chapters we discuss the laser frequency stabilization. Chapter 3 focuses on the Pound-Drever-Hall lock to a Fabry-Perot cavity, while Chapter 4 is on saturation absorption spectroscopy of an Iodine reference cell. In Chapter 5, we will summarize the work and progress we have made towards the doubling system, and discuss what future work is required before we have a working UV MOT.

2 Cavity-enhanced second-harmonic generation with a nonlinear crystal

To obtain enough light at 323 nm for a UV MOT, we need a laser system that produces a sufficient amount of power at 646 nm, and an efficient frequency doubling cavity. We implement our 646 nm laser system with diode lasers and a tapered amplifier, which gives us 250 mW light to couple into the doubling-cavity. For the cavity design, we begin by selecting a nonlinear crystal that optimizes the second-harmonic generation efficiency for our application. Once a crystal has been selected, the optimal laser beam parameters can be calculated. Then, we can design an external cavity, so that the desired beam shape in the crystal is a stable eigenmode of the cavity. At last, the mode-matching condition is determined for the input laser beam to the cavity. We perform a careful measurement of the tapered amplifier output, and use a lens system to mode-match the beam.

First, we should discuss the theory of second-harmonic generation, and use it to guide our design choices.

2.1 Boyd-Kleinman theory of second-harmonic generation

Second-harmonic generation (SHG) is an optical process occurring in a nonlinear medium, in which two photons of the fundamental frequency, ω_1, combine to produce a photon of frequency $\omega_2 = 2\omega_1$. In the nonlinear medium, the relation between the electric field of the applied photons $\mathbf{E}$ and the induced polarization in the medium $\mathbf{P}$ is:

$$\mathbf{P} = \epsilon_0 \chi^{(1)} \mathbf{E} + \epsilon_0 \chi^{(2)} \mathbf{E}^2 + O\left(\mathbf{E}^3\right), \tag{2}$$

in which $\chi^{(1)}$ is the linear susceptibility coefficient, and $\chi^{(2)}$ is in general a rank-3 tensor, accounting for spatial anisotropy of the medium. Substituting the expression for a monochromatic light field, $E = A\cos(\omega t - kz)$, into Eq. (2) gives us:

$$P(z,t) = \epsilon_0 \chi^{(1)} A \cos(\omega t - kz) + \frac{1}{2}\epsilon_0 \chi^{(2)} A^2 \left(1 + \cos(2\omega t - 2kz)\right) + O(A^3). \tag{3}$$

The second term in Eq. (3) corresponds to a frequency-doubled component, resulting from the mixing of two photons. The magnitude of this component is proportional to the input magnitude squared.

Taking the induced polarization from Eq. (2) into Maxwell's equation leads to a differential equation for the second-harmonic field. The case in which the input beam is a plane wave is considered in Ref. [26]. The second-harmonic power is calculated as:

$$P_{2\omega} = \frac{2\pi^2 d_{\text{eff}}^2 l^2}{\lambda_2^2 n_2 n_1^2 \epsilon_0 c} \text{sinc}^2\left(\frac{\Delta k l}{2}\right) P_\omega^2, \tag{4}$$

in which d_{eff} is the effective nonlinear coefficient of the medium, λ_2 is the wavelength of the second-harmonic field, n_1 and n_2 are the index of refraction of the medium for the fundamental and second-harmonic field, respectively, l is the medium length, and $\Delta k = k_2 - 2k_1$ is the difference wave vector. Here $k_{1,2} = 2\pi n_{1,2}/\lambda$ is the wave vector inside the nonlinear crystal.

Eq. (4) shows that minimizing Δk results in maximizing the power of the second-harmonic beam. This is a known as the phase-matching condition. From a physical perspective, if $\Delta k \neq 0$, then the phase velocity of the second-harmonic field is different from that of the fundamental field. At every infinitesimal slice of the medium Δl, the induced second-harmonic field is in-phase with the fundamental field, and the resulting phase difference of the second-harmonic field from different slices leads to destructive interference, reducing the generated harmonic power.

To ensure that the phase-velocity is the same for the fundamental and the second-harmonic field, the indices of refraction must be equal for the two frequencies. Many nonlinear crystals are uniaxial, which means that the index of refraction is different in one direction (extraordinary) from the other two directions (ordinary). As shown in Fig. 3, a technique called critical-phase matching utilizes the angle dependence of the index of refraction. In Type-I phase matching, the polarization of the fundamental beam is aligned with the ordinary axis, Y, and the polarization of the second-harmonic is in the plane perpendicular to Y. If the angle, θ, between the beam axis, k, and the crystal axis, Z, is varied, the index of refraction in the XZ plane, n_e, traces out an ellipse. Meanwhile the index of refraction in the Y axis, n_o, does not vary with θ and traces out a circle. The angle at which $n_o(\omega) = n_e(2\omega)$ should be used for critical phase-matching. Type-II phase matching refers to the case where the two fundamental photons have different polarizations. An example of SHG of 1064 nm using type-II phase matching can be seen in Ref. [27]. In general, in type-I and type-II phase matching, the angle tolerance for successful SHG is usually very small, hence the name critical phase-matching. Another drawback is that,

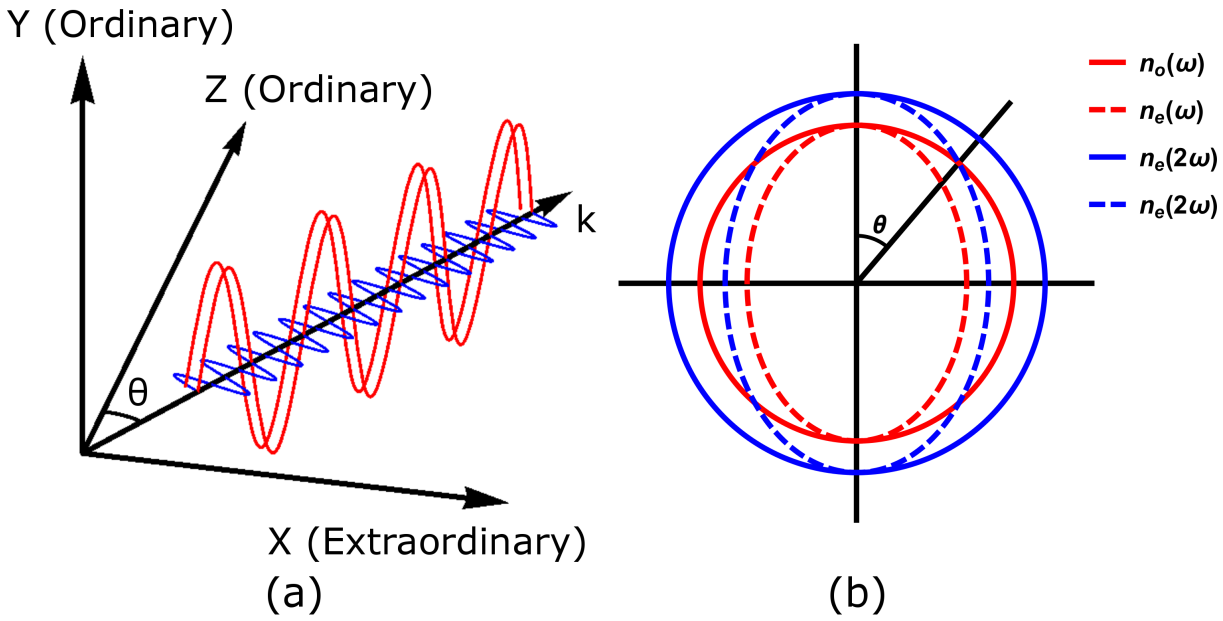

Figure 3: Critical phase-matching schematics. **a**. Type-I phase matching in a uniaxial crystal. The two fundamental beams are o-polarized and the second-harmonic beam is e-polarized. The angle, θ, between the beam axis, k, and the crystal axis, Z, is adjusted for phase-matching. **b**. Refractive indices for the fundamental and second-harmonic beam as a function of the angle θ. The phase-matching angle is determined by the condition that $n_o(\omega) = n_e(2\omega)$.

since the beam axis is not along the crystal axis, the birefringence of the crystal results in a small walk-off angle ρ between the fundamental and second-harmonic beams.

Another technique called noncritical phase-matching uses the temperature dependence to match $n_o(\omega)$ with $n_e(2\omega)$. In this case the beam propagates along the crystal axis with no birefringent walk-off. The angle tolerance for this method is usually much larger compared to critical phase-matching; however, only certain frequencies can be phase-matched with temperature.

So far, we have restricted the discussion to plane waves, whose intensity is constant, whereas real laser beams are Gaussian. Boyd and Kleinman [28] examined Type-I phase-matching for a circular Gaussian beam with walk-off. Their approach is demonstrated in Fig. 4. Conceptually, the crystal is divided into infinitesimal slices, dz, and the second harmonic generation at each slice can be derived using Maxwell's equation. Then, from each slice, the second harmonic field propagates through the crystal to arrive at an observation plane, where the beam profile is computed by coherent superposition from the contributions of all of the slices. The

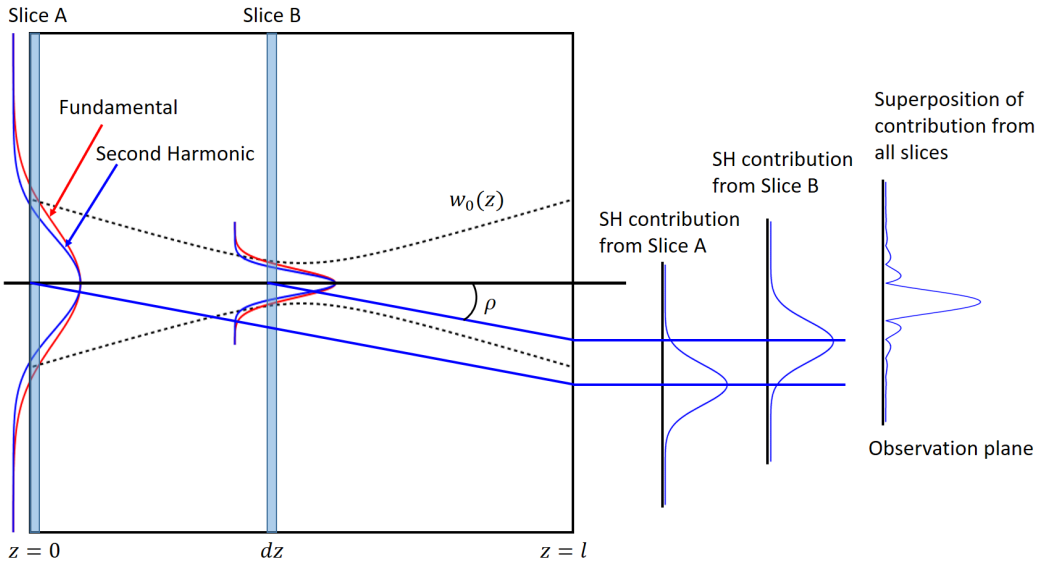

Figure 4: SHG of a focused Gaussian beam in a crystal of length l. The fundamental and second-harmonic beam intensity profile at two slices of the crystal are shown. The dashed curve is the $1/e$ radius of the fundamental beam. The second harmonic beam propagates with a walk-off angle, ρ, relative to the fundamental beam. The observed intensity profile of the second-harmonic beam is the coherent superposition of the contributions from all slices of the crystal.

output second-harmonic power is given by

$$P_{2\omega} = \frac{16\pi^2 d_{\text{eff}}^2}{\epsilon_0 c \lambda_1^3 n_2 n_1} e^{(-\alpha_1 + \frac{1}{2}\alpha_2)l} l h(\sigma, B, \xi) P_\omega^2 \tag{5}$$

in which α_1 and α_2 are the absorption coefficients at the fundamental and second-harmonic frequencies. The function h is a numerical factor that determines the SHG efficiency from beam parameters in a crystal. The arguments of h are $\sigma = b\Delta k/2$, the phase-mismatch parameter, $B = \rho\sqrt{lk_1}/2$, the birefringent parameter, $\xi = l/b$, the beam focus parameter, and $b = 2\pi n_1 w_0^2/\lambda$, the confocal parameter. Chen et al. [29] gives an integral evaluation of h

$$h(\sigma, B, \xi) = \frac{1}{4\xi} \int_{-\xi}^{\xi} \int_{-\xi}^{\xi} \frac{e^{i\sigma(\tau-\tau')} e^{B^2(\tau-\tau')^2/\xi}}{(1+i\tau)(1-i\tau')} d\tau d\tau'. \tag{6}$$

To maximize the SHG efficiency, the phase-mismatch parameter σ is varied to maximize h for a given pair (B, ξ). Note that with a Gaussian beam, it is no longer necessary that $\Delta k = 0$. We define $h_m(B, \xi) = \max\left(h(\sigma, B, \xi)\right)_\sigma$, and Fig. 5 (a) shows h_m for B from 0 to 16, and ξ from 0.1 to 100. The parameter ξ, for a fixed crystal length, is a measure of the tightness of the beam focus inside the crystal. A tightly focused Gaussian beam (small ξ) has a higher peak intensity but a faster rate of beam expansion than a loosely focused one. It is found that the optimum ξ

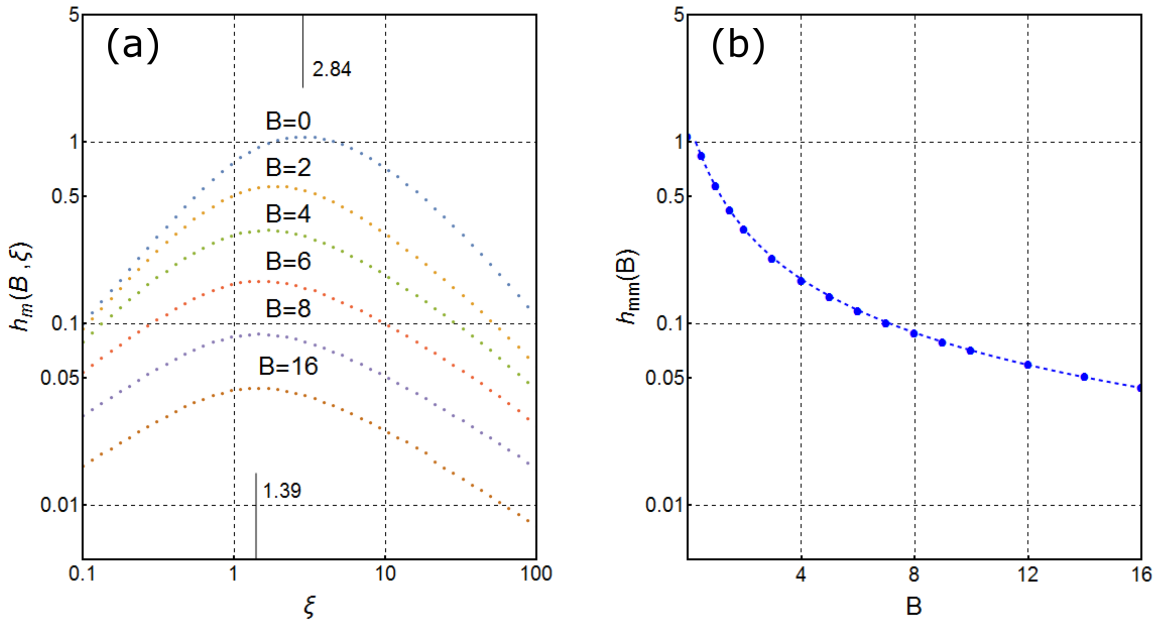

Figure 5: **a**. The Boyd-Kleinman h function $h_m(B,\xi)$. For $B = 0$ the optimal ξ is 2.84, and for large B the optimal ξ is 1.39. **b**. The optimized h function $h_{mm}(B)$. The dotted line is the empirical formula in Eq. (7).

lies between 2.84 for $B = 0$ and 1.39 for very large B. However, note that the tolerance of ξ is large, for example, in the $B = 0$ case, h_m is within 10% of its peak value for $1.5 < \xi < 5.3$. Fig. 5 (b) shows the optimal h_m value given by $h_{mm}(B) = max(h_m(B,\xi))_\xi$. It is fit to an empirical formula

$$h_{mm}(B) = \frac{1.068}{1 - 0.7\sqrt{B} + 1.62B}. \tag{7}$$

This equation is useful for calculating the highest power level achievable given a crystal selection and a cavity design.

As an example, for a 10 mm beta-barium borate (BBO) crystal and 646.7 nm input beam, the walk-off angle $\rho = 78.93$ mrad, $d_{\text{eff}} = 1.93 \times 10^{-12}$ m/V, and the phase-matched index of refraction is 1.666. The absorption coefficients are small so the exponential term in Eq. (5) can be omitted. In this case $B = \frac{\rho}{2}\sqrt{l2\pi n_1/\lambda} = 15.9$ rad, the optimum $\xi = 1.42$ which corresponds to a beam waist $w_0 = 21$ μm. Let us define E_{sp},

$$E_{sp} = \frac{16\pi^2 d_{\text{eff}}^2}{\epsilon_0 c \lambda_1^3 n_2 n_1} e^{(-\alpha_1 + \frac{1}{2}\alpha_2)l} l h_{mm}(B), \tag{8}$$

such that $P_{2\omega} = E_{sp} P_\omega^2$. Then for this crystal we have $E_{sp} = 1.3^{-4}$ W^{-1}, i.e. for 1 W input light, a single pass through the crystal generates 0.13 mW of second-harmonic light.

2.2 Nonlinear Crystal selection

The design of the frequency doubling system begins with nonlinear crystal selection. From the discussion in Sec 2.1, a desirable nonlinear crystal should have the following properties. First, it must be phase-matchable for SHG at the design wavelength. In general, a small walk-off angle is preferred because the $h_{mm}(B)$ function is inversely proportional to ρ. Second, the crystal should have a high nonlinear coefficient, since the second-harmonic power is proportional to d_{eff}^2. Third, the crystal should be transparent to both the fundamental and the second-harmonic frequencies. At last, the thermal properties of the crystal should be in such a way that the thermal lensing caused by the absorption of light will not seriously affect the SHG efficiency [42].

Over 60 nonlinear crystals are commercially available. Their birefringence properties, nonlinear coefficients for each crystal axis, and absorption coefficients have been measured and can be found from manufacturer catalogs and literature. Therefore, for each crystal it is possible to look at the angle and temperature dependence of the refractive indices to determine the phase-matching condition, the effective nonlinear coefficients, etc. Luckily, a free program SNLO [30] has been written to provide the answer automatically. In the function "Qmix", we can select a crystal and input the wavelength of the fundamental beam, and the phase-matching properties are calculated by the program. With this program, we can quickly narrow down the range to a few possible candidates.

We find that none of the crystals are phase-matchable at 646 nm using non-critical phase-matching. With critical phase-matching, we list a few of the crystals that look promising. The last column lists the quantity $h_{mm}(B)d_{\text{eff}}^2/n^2$ for a 1 cm crystal ($B > 1$ for all the crystals listed).

Name	Phase-matching type	d_{eff} (pm/V)	walk-off (mrad)	Index of refraction	$h_{mm}(B)d_{\text{eff}}^2/n^2$
BBO	Type-I	1.93	78.93	1.666	0.163
LiIO3	Type-I	5.05	79.38	1.88	0.301
LBO	Type-I	0.559	18.6	1.616	0.023
KDP	Type-I	0.367	28.79	1.507	0.008
CLBO	Type-I	0.609	38.26	1.493	0.016

Table 1: A list of selected nonlinear materials. The data is acquired from SNLO [30].

Of these crystals, BBO and $LiIO_3$ (lithium iodate) stands out for their large nonlinear coefficients. One drawback for the $LiIO_3$ is that it is very hygroscopic, which could affect its

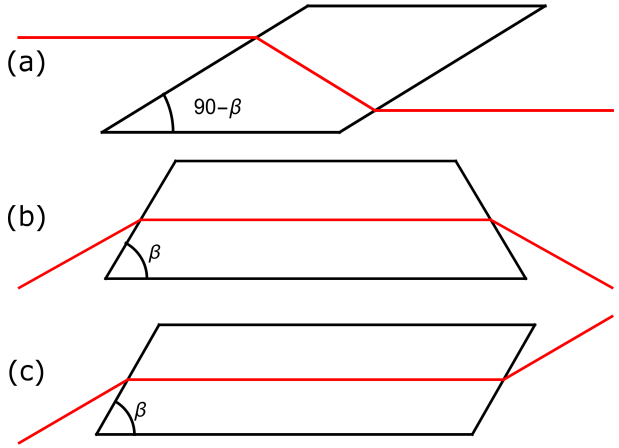

Figure 6: Three types of Brewster-cut crystal. β denotes Brewster's angle. **a**. The cut is at $90° - \beta$. The beam does not propagate along the crystal axis. **b**. The cut is at Brewster's angle. Because the input and output beams are not parallel, a traveling wave cavity with two curved mirrors can be formed with this configuration. **c**. The cut is at Brewster's angle. The input and output faces are parallel.

lifetime. Another problem is that $LiIO_3$ is less transparent at 323 nm than BBO. LBO (lithium triborate), KDP (potassium dihydrogen phosphate), and CLBO (cesium lithium borate) have smaller walk-off angle than BBO; however, their nonlinear coefficients are too small compared to the other crystals. Thus we have decided to use a BBO crystal. We choose a crystal length of 10 mm. The choice involves the external cavity, so it is discussed in Sec. 2.4.

Another important consideration is the crystal cut. Since Type-I phase matching is used, the fundamental light polarization is in the ordinary direction. We can orient the crystal such that this direction coincides with p-polarization, so that the crystal can be cut at Brewster's angle, to minimize reflection loss. Since the second-harmonic is s-polarized, we need to apply anti-reflection (AR) coating to the output end. The coating reduces reflection loss at 323 nm while it does not affect the Brewster condition for 646 nm. Three types of Brewster cut crystals are available, and they are shown in Fig. 6. The angle β defines Brewster's angle. In Fig. 6 (a), the light does not propagate in parallel with the crystal direction, therefore the crystal cross section needs to be large enough to avoid clipping the beam. The crystals in Fig. 6 (b) and (c) do not have this problem. With (b), it is possible to form a traveling wave cavity with two curved mirrors only.

At last, we need to consider the thermal properties of the crystal. The absorption of photons results in heating of the crystal, which affects the refractive index and changes the phase-

matching condition. However, since the amount of heating depends on the input optical power, and the power is determined by the laser system and the doubling cavity, we will discuss the issue of thermal lensing in Sec. 2.6.

2.3 External cavity design

From the calculation at the end of Sec 2.1, we see that for a BBO crystal, a single-pass is insufficient to produce the power we need. Therefore, an external cavity is required. Optical cavities admit beams with particular frequencies and spatial modes, called eigenmodes, which circulate within the cavity and accumulate power. In this section we go through the design procedure for our external cavity. The discussion will focus on how to determine the cavity geometry to accommodate the optimal Gaussian beam for SHG. We will also go over the impedance-matching condition and the cavity enhancement of SHG.

The two types of external cavity used in SHG experiments are the standing wave cavity and the ring cavity. In a standing wave cavity, the nonlinear crystal is placed in the center of two mirrors, and the fundamental beam goes through the crystal from both directions, whereas in a ring cavity, the fundamental beam propagates through the cavity in one direction only. In a standing wave cavity, light will be directly reflected back to the laser, affecting its stability. In addition, because the light passes through the crystal twice, the round trip loss of the standing wave cavity is higher than that of a ring cavity. This will cause a reduction on the SHG conversion efficiency, which is discussed in Sec. 2.4. Furthermore, since the second-harmonic light is generated in two directions, we either have to take extra steps to recombine them, or just use the beam in one direction. Due to these setbacks, we decided to build a ring cavity.

Fig. 7 (a) shows the geometry of the ring cavity, which consists a pair of concave mirrors to focus the beam inside the crystal, and two flat mirrors to form a stable resonator. We assume that the cavity is symmetric, i.e. the incidence angles of the four mirrors are the same, and the distances between the crystal surfaces and the curved mirrors are the same ($AB = EF$). The design procedure follows the steps outlined below [32].

First, a crystal is selected. The crystal length, the phase-matching angle, and the crystal cut are determined, and the optimal confocal parameter, b, can be calculated from the Boyd-Kleinman theory. Second, if we assume that the focal position in the crystal is at the crystal

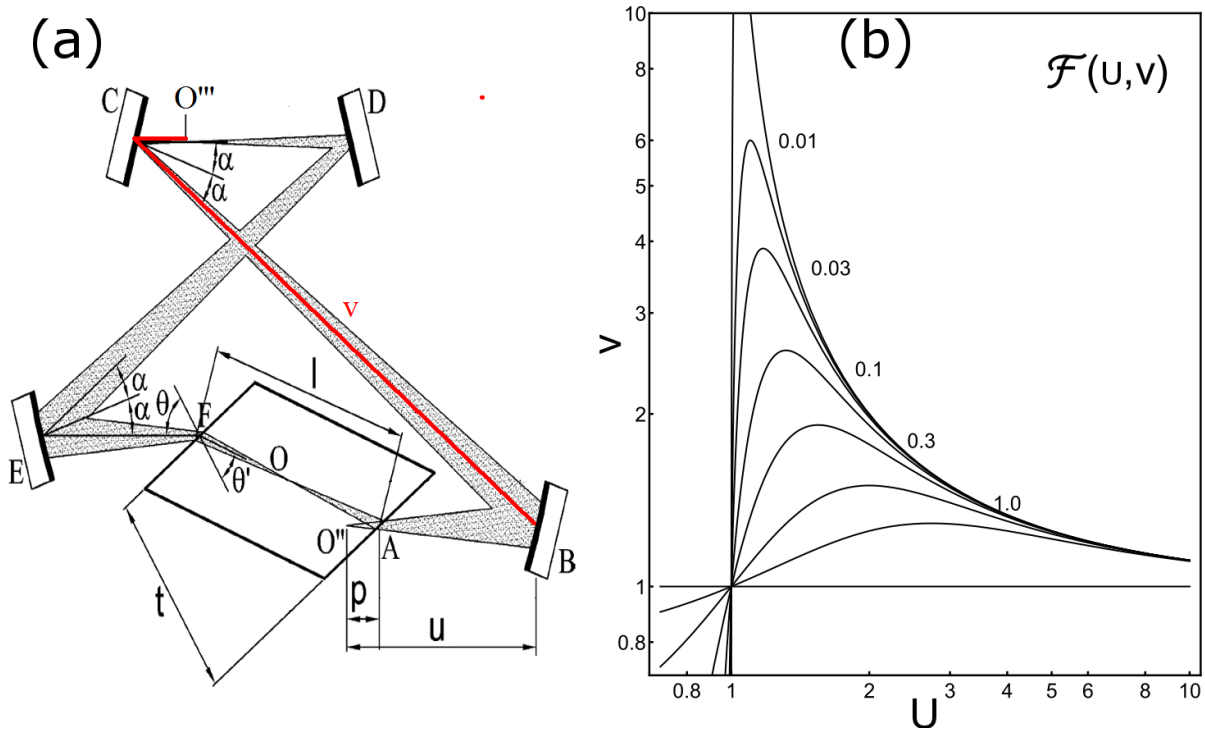

Figure 7: **a**. Geometry of the ring cavity. This figure is reproduced from [32]. **b**. Contours of the $\mathcal{F}$ function. Region with positive $\mathcal{F}$ corresponds to a stable cavity.

center, O, there is a virtual beam waist location, O'', and beam parameter, b''. This corresponds to the apparent beam waist when viewed from outside of the crystal. Note that the beam propagation within the crystal introduces astigmatism because the beam is incident at Brewster's angle. We use the non-zero incidence angle, α of the curved mirror to compensate for the astigmatism [33]. With the virtual beam parameter, b'', and the concave mirror focal length, f, we solve the cavity stability equations to derive the incidence angle, α, to the curved mirror, the distance, u, from the virtual waist O'' to the concave mirror, B, and the optical path length, v, from the secondary waist, O''', to B. Then, all the rest of the cavity dimensions can be calculated using the symmetry of the cavity.

The crystal selection and waist size calculation are already discussed in Sec. 2.1 and 2.2. With the optimal waist, w_0, the confocal parameter is given by:

$$b_{x,y} = \frac{2\pi w_0^2 n}{\lambda_1}, \tag{9}$$

in which λ_1 is the vacuum wavelength of the fundamental beam, and n is the crystal refractive index. The subscript, x and y denotes the sagittal and tangential planes, respectively. The distances between the virtual waist, $O''_{x,y}$, and the curved mirror, B, is denoted by $u_{x,y}$ and we

define the average distance $u = \frac{1}{2}(u_x + u_y)$. For a Brewster-cut crystal, the astigmatism $z = u_x - u_y$ and the beam parameter $b''_{x,y}$ are given by [32]:

$$z = \frac{t}{2n^4}\sqrt{1+n^2}(n^2-1), \tag{10}$$

$$b''_x = b_x/n, \tag{11}$$

$$b''_y = b_y/n^3, \tag{12}$$

in which $t = ln/\sqrt{1+n^2}$. With the virtual confocal parameter and astigmatism determined, the next task is to solve the cavity stability equation to calculate the distances u and v from the two waist locations to the mirror, B, and the incidence angle α to the curved mirror. We introduce a function $\mathcal{F}$ as follows.

$$\mathcal{F}(U,V) = \left(\frac{U-1}{V-1}\right)(1-(U-1)(V-1)) \tag{13}$$

The physical meaning of the function is that, for normal incidence of a curved mirror with focal length f, the beam with a waist, w_0, at a distance, u, from the mirror, should have a secondary waist at a distance, v, satisfying

$$\left(\frac{b}{2f}\right)^2 = \mathcal{F}\left(\frac{u}{f}, \frac{v}{f}\right), \tag{14}$$

in which $b = 2\pi w_0^2/\lambda$ is the confocal parameter. Fig. 7 (b) shows a contour plot of $\mathcal{F}$. The regions where $\mathcal{F}$ is positive corresponds to a stable cavity. When the incidence angle is nonzero, Eq. 14 becomes

$$\left(\frac{b_x}{2f\cos(\alpha)}\right)^2 = \mathcal{F}\left(\frac{u_x}{f\cos(\alpha)}, \frac{v_x}{f\cos(\alpha)}\right), \tag{15}$$

$$\left(\frac{b_y\cos(\alpha)}{2f}\right)^2 = \mathcal{F}\left(\frac{u_y\cos(\alpha)}{f}, \frac{v_y\cos(\alpha)}{f}\right). \tag{16}$$

. We scale the virtual confocal parameters by the concave mirror focal length f, i.e. $X = b''_x/2f$, $Y = b''_y/2f$, $Z = z/2f$. We define the ellipticity as $\mathbf{e} = w_y/w_x$ at the secondary waist. For the incidence angle, we define $\phi = \cos(\alpha)$. For the focal distances, we scale them by the focal length, $U = u/f$, $V = v/f$. These parameters are listed in Table 2. Accounting for the nonzero incidence angle, we can derive the following equations [32]:

$$\mathcal{F}\left((U+Z)/\phi, V/\phi\right) = X^2/\phi^2, \tag{17}$$

$$\mathcal{F}\left((U-Z)\phi, V\phi\right) = Y^2\phi^2, \tag{18}$$

$$\frac{\mathcal{F}\left(V/\phi, (U+Z)/\phi\right)}{\mathcal{F}\left(V\phi, (U-Z)\phi\right)} = \frac{1}{\mathbf{e}^4\phi^4}. \tag{19}$$

	Property	True	Scaled
Scale by	Mirror focal length	f	
Define	Tangential beam parameter	b''_x	$X = b''_x/2f$
	Sagittal beam parameter	b''_y	$Y = b''_y/2f$
	Astigmatism	z	$Z = z/2f$
	Secondary waist ellipticity	$\mathbf{e} = w_{y2}/w_{x2}$	
Solve for	Average distance to virtual focus	u	$U = u/f$
	Distance to secondary focus	v	$V = v/f$
	Mirror incidence angle	α	$\phi = \cos(\alpha)$

Table 2: Parameters used to solve the cavity stability equations. This is reproduced from Ref. [32].

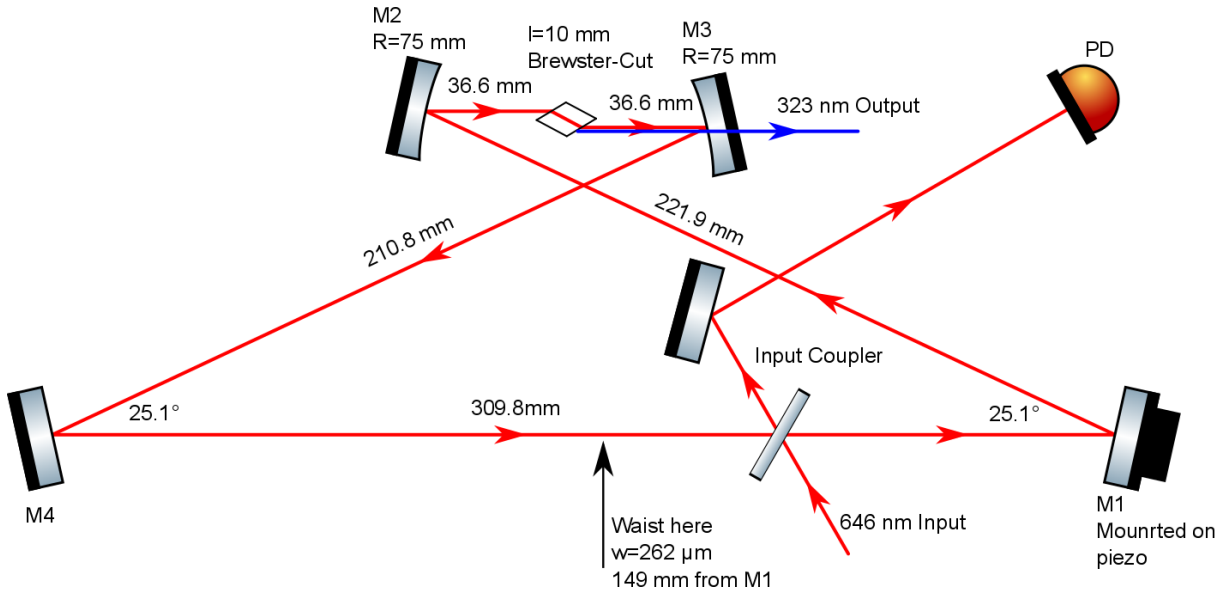

Figure 8: The calculated dimensions for our frequency doubling cavity. A beam sampler is used to couple light with the cavity. The beam sampler has an angle-dependent reflection coefficient, so that the incidence angle can be tuned to achieve impedance-matching.

Eq. 17 and 18 sets the tangential and sagittal confocal parameters at the virtual waist, O'', and Eq. 19 sets the ellipticity at the secondary waist, O'''. For our cavity, we assume no astigmatism at the secondary waist, so $\mathbf{e} = 1$. These equations are solved numerically to find ϕ, U, and V.

Once the focal distances u, v and the mirror incidence angles are found, the rest of the cavity dimensions can be solved using the symmetry of the cavity. From these calculations, our cavity dimensions is shown in Fig. 8.

2.4 Cavity enhancement of the second-harmonic power

To obtain maximum enhancement of the fundamental beam power, the percent of input light entering the cavity should equal to the round trip loss of the cavity, which is the impedance-

matching condition. The cavity round trip loss contains a linear loss, L, from mirror surfaces and absorption in the crystal and a nonlinear loss, N, from SHG. Each mirror has a loss less than 0.1 %, and we estimate a total of 0.3% for the linear loss due to mirrors. Therefore,

$$L = 0.003 + \alpha_1 l. \tag{20}$$

in which α_1 is the absorption coefficient of the crystal at 646 nm, and l is the crystal length. N can be computed from Boyd-Kleinman theory [28].

As shown in Fig. 8, we choose to use a beam sampler to couple the light with the cavity [34]. The beam sampler has an angle-dependent reflection coefficient, which is useful for impedance-matching. Let R denote the reflection of the beam sampler, then the SHG conversion efficiency, $\eta = P_{2\omega}/P_\omega$ is given by an implicit equation [35]

$$\eta = \frac{16R^2 E_{\mathrm{sp}} P_\omega}{\left(2 - \sqrt{1-R}\left(2 - L - \sqrt{\eta E_{\mathrm{sp}} P_\omega}\right)\right)^4}, \tag{21}$$

in which E_{sp} is the single-pass conversion coefficient given in Sec.2.1. The impedance-matching condition is satisfied when the reflection satisfies the following condition:

$$R = \frac{L}{2} + \sqrt{\left(\frac{L}{4}\right)^2 + E_{\mathrm{sp}} P_\omega}, \tag{22}$$

From the above equations, we see that the conversion efficiency is dependent on the crystal length through the linear loss due to absorption. Therefore we choose the crystal length that maximize the conversion efficiency.

It is difficult to measure the precise value of the absorption coefficient α_1, because usually the crystals are short, so the total absorption is comparable to the noise in the power measurement. Based on the UV power from APP3, the absorption coefficient of the BBO crystal is estimated to be 0.1 m^{-1}. Another reported value at this wavelength is 0.22 m^{-1} [36]. Given the absorption coefficient, we plot the optimal SHG conversion efficiency (optimized for impedance matching) as a function of crystal length in Fig. 9. α_1 from 0.1 to 0.3 m^{-1} are included, with the power of the fundamental beam set to 150 mW. We have chosen a crystal length of 10 mm, because it maximize the SHG conversion efficiency if $\alpha_1 = 0.1$ m^{-1}, while remaining within 10% of the peak value for a range of α_1. As a reference, for $\alpha_1 = 0.1$ m^{-1}, $l = 10$ mm, and $P_\omega = 150$ mW, we have $r_{opt} = 0.7\%$, $\eta = 42\%$.

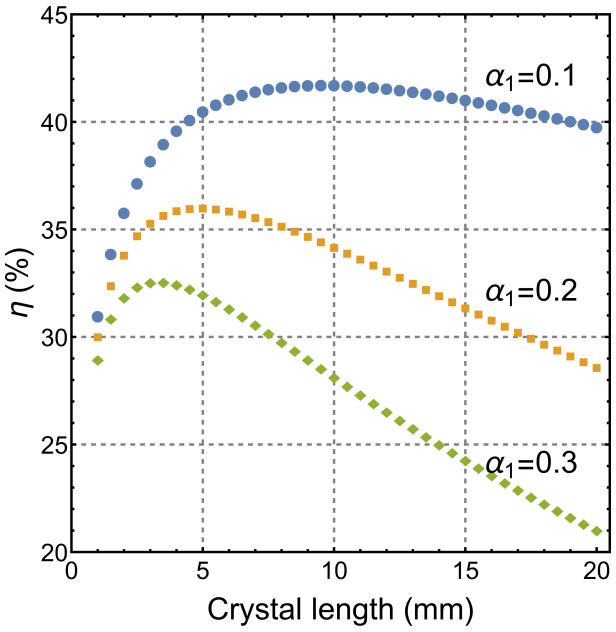

Figure 9: Optimal SHG conversion efficiency as a function of crystal length and absorption coefficient. The fundamental power is 150 mW.

We plot the SHG conversion efficiency and power as a function of input power in Fig. 10. If we can couple 150 mW, we can expect an output of 60 mW, the same power as the commercial system in APP3. We can also compare the calculated power with the 626 nm doubling cavity in Ref. [24]. Their system also uses a 10 mm BBO crystal at Brewster's angle. The material parameters, d_{eff}, n, ρ and α_1 are all within 1% between 646 nm and 626 nm. Their conversion efficiency is 50% for input power greater than 0.3 W.

2.5 Generation and amplification of 646 nm light

With the doubling cavity designed, we need a laser system to generate high power 646 nm light with the proper beam parameters to couple with the cavity. Our system includes a master external cavity diode laser (ECDL) as the source, and two stages of amplification with a slave laser and a tapered amplifier (TA). The complete schematic of the system is shown in Fig. 11.

An ECDL contains a diode laser and an optical grating in Littrow configuration [38]. It is capable of producing a single mode output with a narrow linewidth, and the frequency can be continuously tuned over a large range without mode-hopping. We use an Ushio HL6364DG for the ECDL. It has a center wavelength of 642 nm, but can be tuned to 646 nm with the grating and temperature. The diode current is generated from a home made current controller circuit, which also controls the piezo element that tunes the laser frequency. The laser temperature is

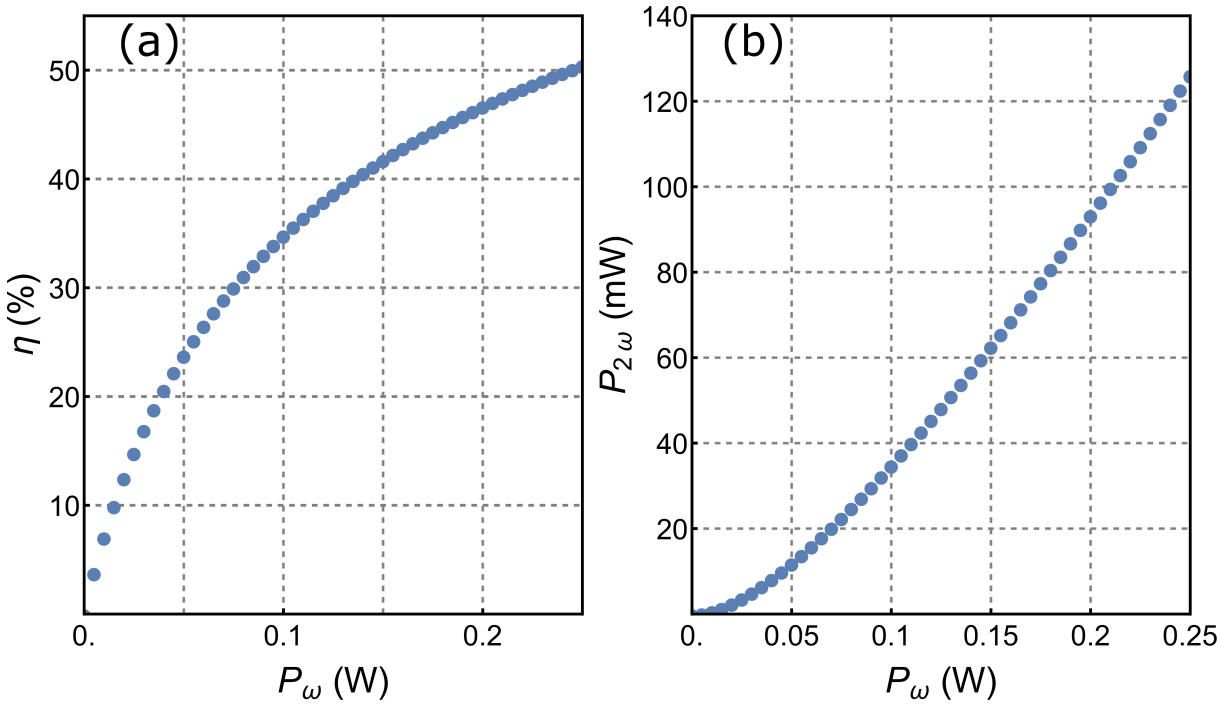

Figure 10: **a**. The conversion efficiency and **b**. the output power as a function of the input power for the impedance-matched cavity.

adjusted by a thermoelectric cooler (TEC), controlled by our ILX Lightwave LDC-3916 laser diode controller.

About 20 mW light passes through an optical isolator. A 10:90 beam splitter sends 2 mW to a Fabry-Perot cavity for frequency stabilization, and 18 mW to inject a slave laser. For the slave laser, we use an Ushio HL6385DG diode, which has an output power of 150 mW. The isolator for the slave laser has a polarization beam splitter (PBS) cube on the output side instead of a polarizer. The half-waveplate and the PBS combination allows the injection light to go through the isolator in the reverse direction, so that we can inject the slave. About 10 mW of the master light is coupled into the slave, and we obtain a maximum power of 75 mW after the isolator. Both the slave current and temperature are controlled by the ILX controller. The slave output is split in three ways. 25 mW is used to inject a second slave laser, which produces the light for the iodine reference cell discussed in Sec 4. 45 mW is used to seed the tapered amplifier, and about 2 mW is coupled to a second Fabry-Perot cavity for spectral analysis.

A tapered amplifier (TA) is a semiconductor laser that has a tapered waveguide section near the output end, as shown in Fig. 12. The device can amplify the input light by about 7.4 dB, or 250 mW for our system. An input lens of f = 11 mm is used to couple the seed light

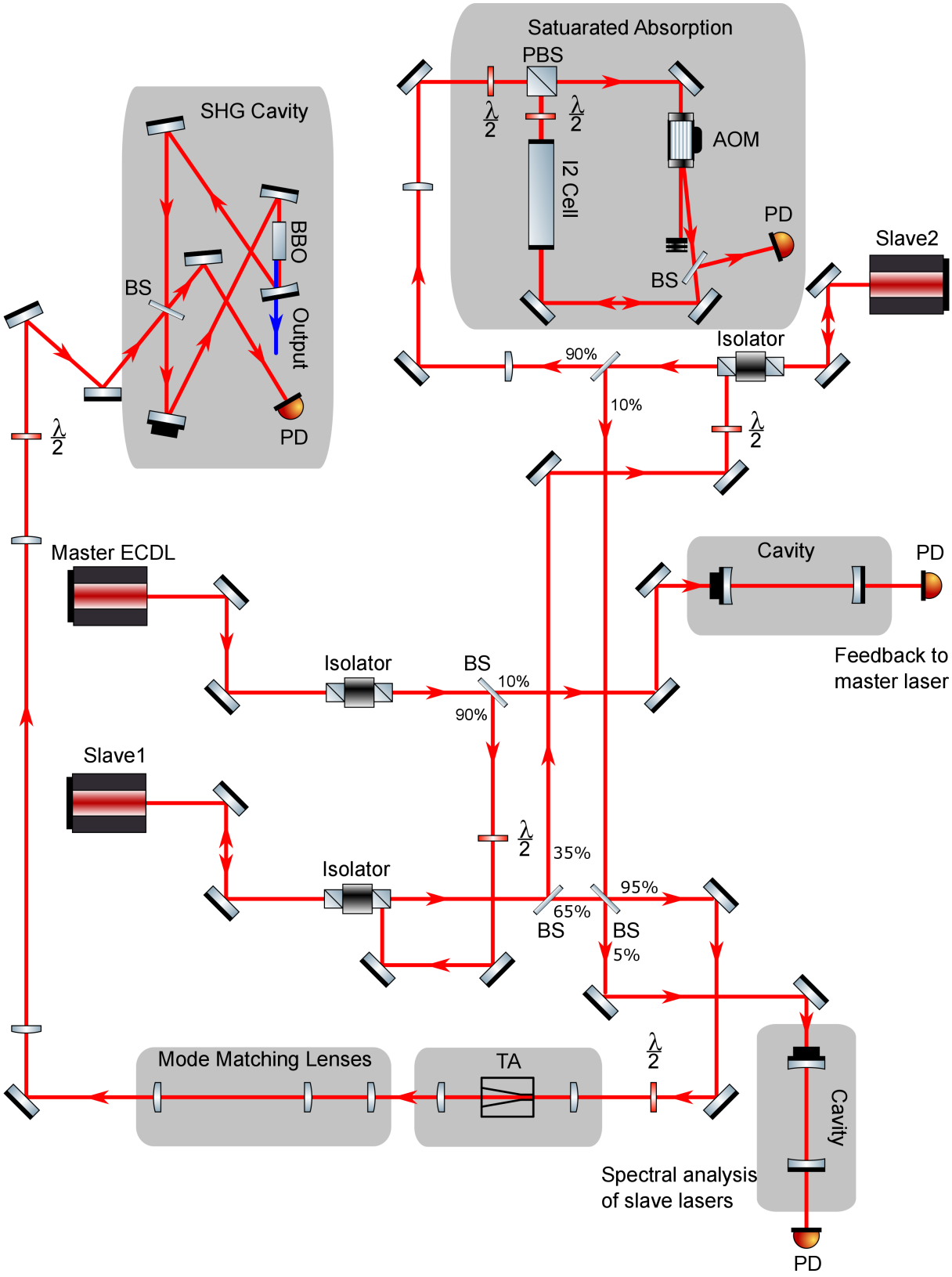

Figure 11: Optical layout of the laser system. $\frac{\lambda}{2}$: half-wave plate. AOM: acousto-optical modulator. BS: beam splitter. PBS: polarization beam splitter. PD: photo diode. TA: tapered amplifier.

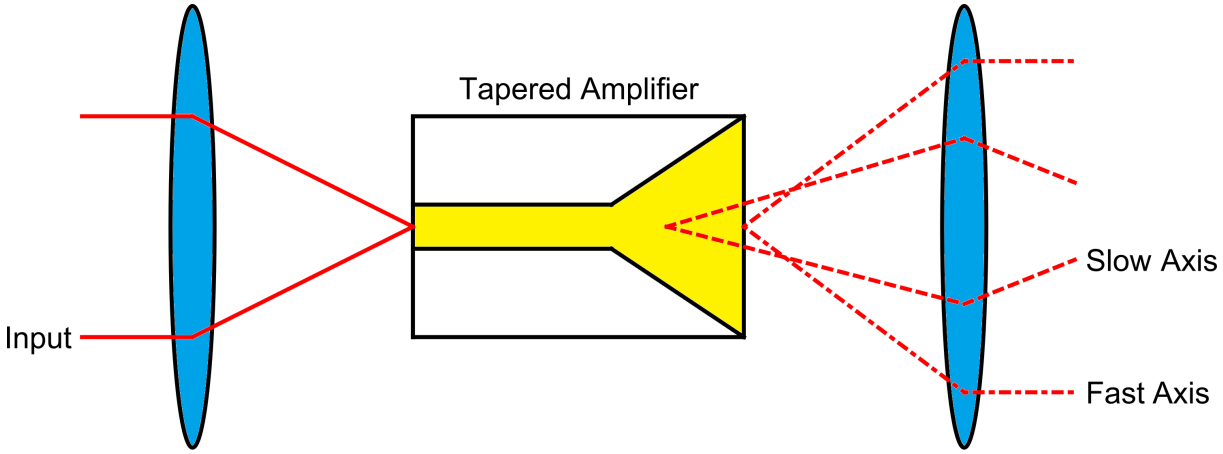

Figure 12: The waveguide section of the TA is shown in yellow. The output beam of the TA exhibits astigmatism and asymmetry. The fast axis (vertical direction) has a focal point at the output facet and a large divergence angle, whereas the slow axis (horizontal direction) has a virtual focal point inside the amplifier and a smaller divergence angle. The output collimating lens only collimates the fast axis.

to the narrow input aperture (7 μm). Due to the spatial asymmetry of the tapered section, the output beam is highly asymmetric and astigmatic. The divergence angle for the horizontal and vertical direction are 14° and 29°, respectively. We use an $f = 8$ mm, $NA = 0.5$ aspheric lens to collimate the fast axis (vertical), and two sets of cylindrical lenses are used to reshape the two directions for mode matching to the doubling cavity.

Originally we put the lenses on 5-axis lens mounts physically separated from the TA mount. Each time the TA was turned on, the output power would decrease within a few minutes. We attributed this to movement of the TA relative to the lenses, due to heating in the TA after turning on the current. Therefore we redesigned the TA assembly, as shown in Fig. 13. The TA and the collimating lenses are mounted on a single brass block whose temperature is adjusted by a TEC below. In this configuration, the relative motion is reduced because the whole system reaches thermal equilibrium together. After the new assembly is built, we find that the TA stabilizes to the same power each time when it's switched on.

To mode-match the TA output to the doubling cavity, two approaches are considered. The first method is to use a single mode polarization maintaining fiber to clean up the spatial mode, and then reshape the beam to the desired waist with a telescope. The merit of this approach is that the output from the fiber is a TEM00 mode, free from any aberration. Furthermore, the fiber coupling separates the doubling cavity module from the TA module, thus changes in the

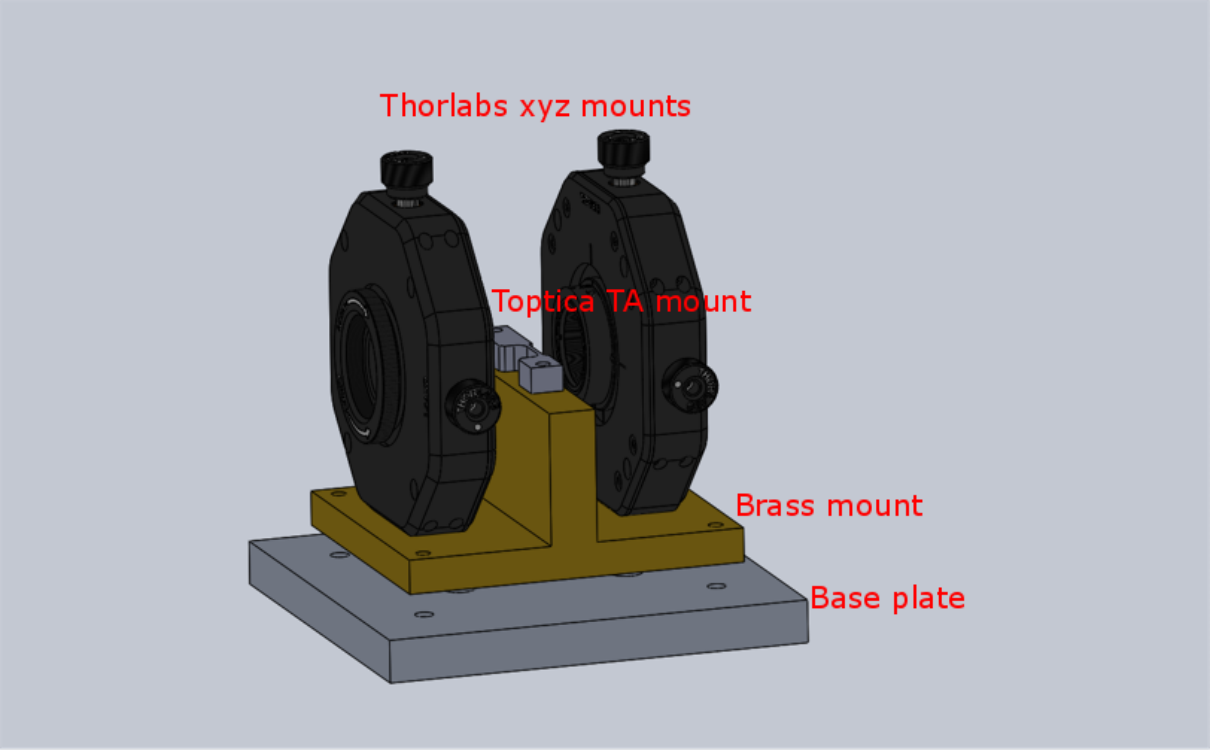

Figure 13: Schematic of the TA assembly. The TA chip is mounted on a Toptica TA mount. The input and output collimating lenses are placed in Thorlab XYZ mounts. A brass piece that holds the TA and lens mounts is designed such that the TA is at the focal position of both lenses. A TEC is placed between the brass mount and an aluminum base plate.

laser system would not affect the cavity alignment. However, the efficiency of fiber coupling is limited by a number of factors. First, the TA beam will need to be symmetric with a waist size specified by the fiber coupler. Second, part of the TA power is distributed in higher order spatial modes, which will not go through the fiber. The coupling efficiency reported in the literature [39] and measured from other TAs in our lab is around 50%. Therefore, at most we expect 120 mW for the doubling cavity, limiting the UV power we could obtain.

The other approach is to shape the TA output to match the cavity mode using cylindrical lenses, and couple into the cavity directly. This is the method used by the commercial system in APP3, and the cavity coupling efficiency is at about 60%. We have decided to copy this approach. Our target is to make the beam waist 262 μm in both directions, and the waist locations at the same location. The schematic for the mode matching setup is shown in Fig. 14. For the vertical direction, the beam is collimated by the output lens (L1), and the beam size is measured to be 3.5 mm. A pair of cylindrical lenses with $f = 200$ mm (L2) and $f = -15$ mm (L3) are used. Because of the large beam size, the distance from L1 to L2 is not important. For

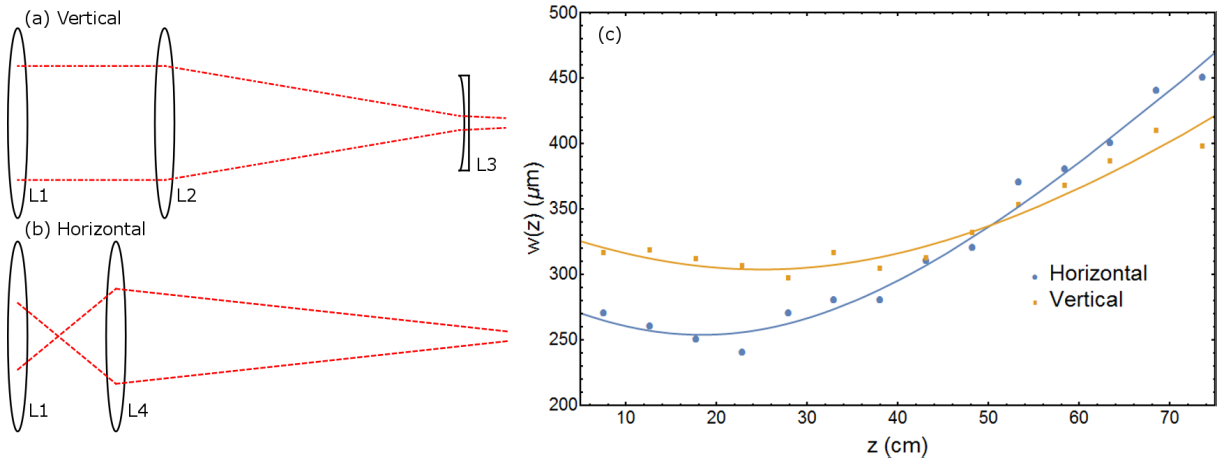

Figure 14: Mode-matching the TA output beam with the doubling cavity. **a**. the vertical and **b**. the horizontal direction beam path after the tapered amplifier. L1 is the output collimating lens of the TA, L2, L3 and L4 are cylindrical lenses. **c**. Measurement of the beam size in the horizontal and vertical direction after the telescope.

the horizontal direction, the beam waist after L2 is measured to be 40 μm. With an f = 60 mm (L4) lens we find that the beam size can be brought to the correct value, but the lens needs to be at slightly larger than 60 mm away from the waist. The waist after L4 is 250 mm from L4. By moving the vertical cylindrical lenses, the two waist locations can be brought together. Note that all the beam measurements assume a Gaussian beam profile, whereas in reality, the vertical beam profile is usually not Gaussian, due to the presence of higher order TEM modes. The M^2 value is 1.3 for the vertical and 1.1 for the horizontal direction. Therefore, the beam sizes we measure are only an approximation.

Because of spatial constraints, we need an additional one-to-one telescope with cylindrical lenses (f = 200 mm) to recreate this beam profile near the cavity. The beam profiles after the telescope are shown in Fig. 14 (c). We can see that the vertical beam size is off by about 20%, and the astigmatism is about 8 cm. Although this is not an ideal situation, spending more time on the beam shaping is not useful because we do not have a perfect Gaussian beam. Eventually, mode-matching into the cavity will determine if the beam profile needs to be adjusted.

To align the beam with the doubling cavity, a photo diode is used to measure the transmitted light from the input coupler, while the cavity length is scanned by a piezo mounted to one of the flat mirrors. Note that neutral density filters should be used to prevent damage of the photo diode. When no light is coupled in the cavity, a constant voltage is measured, corresponding to the power transmitted through the input coupler. A dip will appear when some light is coupled

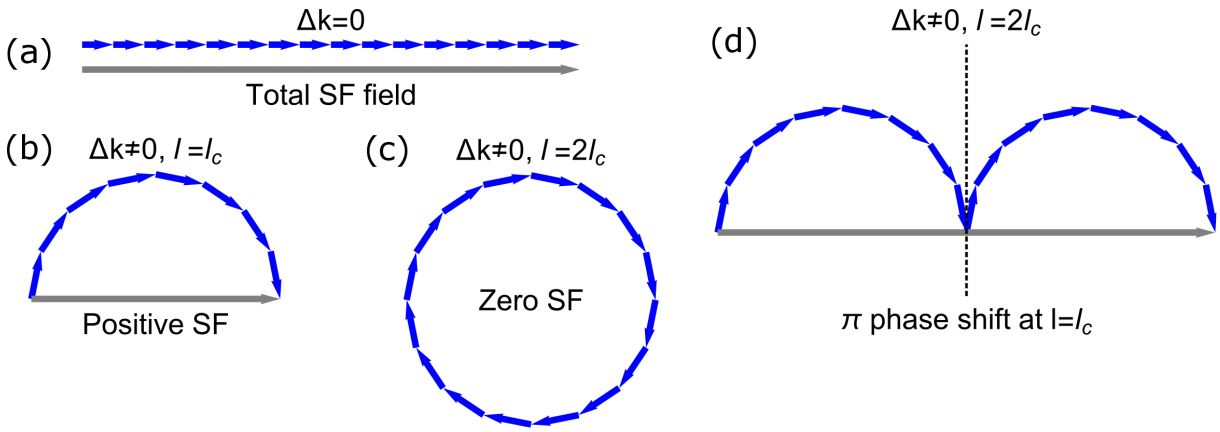

Figure 15: **a**. When $\Delta k = 0$, the SH electric field vectors from all slices (blue arrows) are in phase, thus the total field strength (gray arrows) is maximized. **b**. When $\Delta k > 0$, there is a phase difference between the electric field from each slice. Over a distance l_c, the phase has changed π, and the total field strength is positive. **c**. Over a distance $2l_c$, due to the destructive interference the total SH field is zero. **d**. When a π phase-shift is introduced at l_c, the total SH field is again positive.

in, because at the input coupler, the reflected light from the cavity is out-of-phase with the transmitted input light. This is due to the Stokes relation, which requires the reflection phase shift of the two sides of the beam coupler to differ by π [40]. When the impedance matching condition is met, and all the light is coupled in the cavity, the bottom of the dip will go to zero, because the reflected cavity light and the transmitted input light have the same amplitude. Therefore, the dip size normalized by the background DC is a measure of the coupling efficiency. To optimize the coupling, we need to iteratively adjust the input coupler angle, the crystal angle, and the mirror pointing. Currently, the input coupling efficiency remains below 20%.

2.6 Sum Frequency generation for 646 nm

In this section, we discuss an alternative approach to obtain light at 646 nm. As mentioned in the introduction, Wilson et al. [24] uses fiber lasers to produce 5 W each of 1550 nm and 1051 nm light. A Periodically-poled lithium niobate (PPLN) crystal is used to generate 2 W of 626 nm light by sum frequency generation (SFG). This method can be adapted to produce light at 646 nm. In Ref. [25], 4 W of 1550 nm light and 1.6 W of 1110 nm light are combined in a PPLN crystal to produce 800 mW of 646 nm light.

Instead of matching the refractive indices for the input beams to achieve phase-matching, the PPLN crystal uses a technique called quasi-phase-matching (QPM). To understand the work-

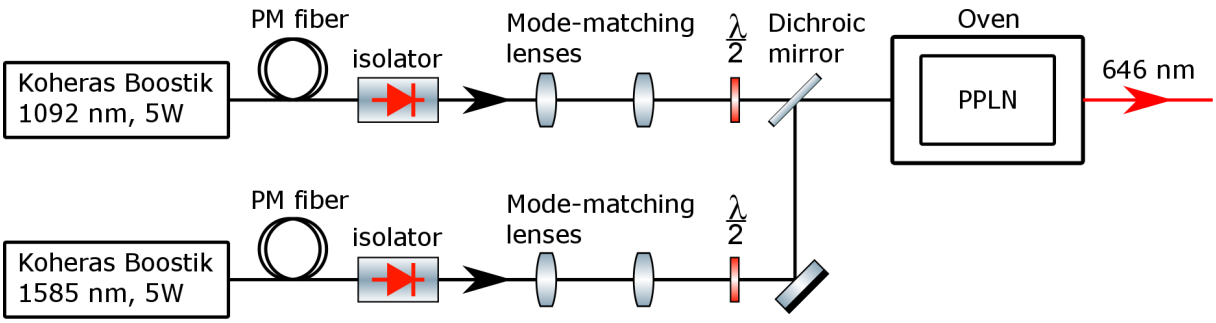

Figure 16: Our plan for the sum frequency generation to produce 646 nm light. The design is adapted from [24].

ing principle of QPM, we refer to the treatment of the plane wave SHG in Sec. 2.1. Note that SHG is a special case of SFG, so here we refer to the output as the sum frequency (SF). The wavevector difference is $\Delta k = k_3 - k_1 - k_2$, where k_1 and k_2 are the wavenumber for the two input frequencies and k_3 is the wavenumber for the SF. As from before, we assume that the crystal is divided into thin slices of width Δz, and the total SF is a superposition of SF contribution from all the slices. Since the intensity of the fundamental beam is constant, the SF electric field generated at each slice has the same magnitude. Each component has a relative phase $\Delta\phi = \Delta k \Delta z$ from the previous component. When we have perfect phase-matching, i.e. $\Delta k = 0$, all components are collinear, and the total SF is maximized, as shown in Fig. 15 (a). On the other hand, with a nonzero Δk, over a crystal length $l_c = \pi/\Delta k$, the SF components interfere constructively, as shown in Fig. 15 (b). However, when the crystal length is $2l_c$, the overall SF is zero because of the completely destructive interference, as shown in Fig. 15 (c). In QPM, the crystal structure is engineered such that the beam encounters a -phase shift whenever $z = nl_c$, for an integer n. With this construction, an overall positive SH can be achieved, as shown in Fig. 15 (d). QPM allows SHG and SFG to occur in materials that do not have a phase-matching condition based on their birefringent properties. In many cases, materials with large nonlinear coefficients, that do not have a birefringent phase-matching condition, can be used in QPM. In addition, QPM does not require any angle tuning, and there is no birefringent walk-off.

We have planned for a laser system that uses QPM for SFG of 646 nm, as shown in Fig. 16. The two input beams are at 1092 nm and 1585 nm, provided by NKT Koheras Boostik fiber lasers, each rated for 5 W. The laser output is fiber-coupled with polarization-maintaining fibers. The laser beams are mode-matched with two separate telescopes, and are combined by

a dichroic mirror. A 40 mm long PPLN crystal, manufactured by Covesion, is used for SFG for 646 nm [41]. Below we show a list of the main components in this plan, and their price estimations.

Item	Manufacturer	Price estimate (USD)
Fiber laser (1585 mn, 5 W)	NKT	45k
Fiber laser (1092 nm, 5 W)	NKT	47k
PPLN, oven and mount	Covesion	6k

Table 3: A list of the main components of the SFG approach for 646 nm light and their price estimations.

We can estimate the 646 nm power by comparing to the efficiency obtained in Ref. [24,25]. The efficiency η is defined as

$$\eta = \frac{P_3}{P_2 P_1 l}, \tag{23}$$

in which P_3 is the output power, and P_1, P_2 are the two input powers. l is the crystal length. The 626 nm SFG measures a conversion efficiency $\eta = 0.027\ \mathrm{W^{-1}cm^{-1}}$ [24], and the 646 nm SFG has a conversion efficiency of $0.03\ \mathrm{W^{-1}cm^{-1}}$ [25]. Because of the proximity of the input wavelengths used in these experiments, we should expect that the efficiency of our setup is very close to these reported values. For our system, if 4 W of each of the two input is used, we should expect an output power at around 1.7 to 1.9 W.

To obtain 323 nm light, the doubling cavity that we have designed in Sec. 2.3 can be used, provided that we mode-match the SFG output beam to the cavity eigenmode. Since the input power will be almost an order of magnitude greater than the TA power, we need to consider the problem of thermal lensing. The crystal absorbs about 0.1% of the circulating power in the cavity. Assuming a 1.5 W input power, then the circulating power is about 90 W at the impedance-matching condition. Therefore about 90 mW is absorbed by the crystal, causing heating of about 1.5 K along the beam path. The rise in temperature changes the refractive index, and as a result the phase-matching condition is affected. This property has been examined in [42]. It was found that up to a certain power level, the thermal lensing effect can be compensated by adjusting the distance between the curved mirrors and the nonlinear crystal. Wilson et al. has found that only for input power higher than 1.5 W, the conversion efficiency begin to significantly diverge from the theoretical curve [24].

3 Locking the master ECDL to a Fabry-Perot cavity

For a successful UV MOT, the laser frequency must be actively stabilized, so that the laser linewidth is smaller than the transition linewidth, and the center frequency is kept fixed relative to the atomics transition. To achieve this, we have implemented a two stage locking scheme to stabilize the master laser frequency. The first stage uses a Pound-Drever-Hall technique to lock the laser to a Fabry-Perot (FP) cavity. In the second stage, the FP cavity is locked to an iodine transition that is close to half the frequency of the ^{7}Li 2s-3p line.

A Fabry-Perot cavity is formed by two highly reflective mirrors. If the cavity length is an integer multiple of half the light wavelength, i.e. $l = N\frac{\lambda}{2}$, then the light can form a standing wave inside the cavity. Otherwise, for each successive round trip the light acquires a nonzero phase difference, and destructively interfere. The transmission of the cavity, $T = P_{tr}/P_{in}$, as a function of frequency is shown in Fig. 17 (b). The frequency difference between two successive peaks is defined as the free-spectral range (FSR). For a given cavity length, l, $f_{\text{fsr}} = c/4l$ for a confocal cavity. The $4l$ in the denominator is the cavity round trip path length for the confocal cavity. The cavity finesse is defined as the ratio of the free spectral range to the full width half maximum (FWHM) of each peak. For a given mirror reflectivity R, the finesse is $\pi R^{1/2}/(1-R)$ for a confocal cavity [37].

The free-running laser frequency can be unstable due to a number of factors including temperature fluctuation, phase-noise, and laser gain-dynamics. Stabilizing the laser frequency with a resonance mode of a high finesse cavity can significantly reduce the laser linewidth. The Pound-Drever-Hall (PDH) technique [43, 44] uses phase modulation of the laser light to create sidebands. The reflected light from the cavity is measured. This signal is mixed with the phase modulation signal, and an error signal is obtained by low pass filtering the mixed signal. This error signal has a zero-crossing located at the center of the resonance mode. With this technique, ideally the locked laser linewidth is limited only by the shot noise in the reflected sideband power.

The derivation of the error signal is quite straightforward. For a laser beam with frequency ω, when the phase is modulated with amplitude β and frequency Ω, the electric field is given by

$$E_{\text{in}} = E_0 e^{i(\omega t + \beta\cos(\Omega t))}. \tag{24}$$

When the modulation amplitude β is small compared to unity, the electric field can be approximated by

$$E_{\text{in}} = E_0 e^{i\omega t} + E_1 e^{i(\omega+\Omega)t} - E_1 e^{i(\omega-\Omega)t} \tag{25}$$

Let $P_{0,1} = |E_{0,1}|^2$ be the power in the main carrier and the sidebands. We can assume that all the power in the laser beam are in these three frequencies. The reflected beam is represented by

$$E_{\text{ref}} = F(\omega)E_0 e^{i\omega t} + F(\omega+\Omega)E_1 e^{i(\omega+\Omega)t} - F(\omega-\Omega)E_1 e^{i(\omega-\Omega)t}, \tag{26}$$

in which the F function is given by

$$F(\omega) = R\frac{\left(\exp\left(i\frac{\omega}{\nu_{\text{fsr}}}\right) - 1\right)}{1 - R^2\exp\left(i\frac{\omega}{\nu_{\text{fsr}}}\right)}. \tag{27}$$

A photo diode measures the reflected power, given by

$$\begin{aligned} P_{\text{ref}} =& P_0|F(\omega)|^2 + P_1\left\{|F(\omega+\Omega)|^2 + |F(\omega-\Omega)|^2\right\} \\ &+ \sqrt{P_0P_1}\{\text{re}\left[F(\omega)F^*(\omega+\Omega) - F^*(\omega)F(\omega-\Omega)\right]\cos(\Omega t) \\ &+ \text{im}\left[F(\omega)F^*(\omega+\Omega) - F^*(\omega)F(\omega-\Omega)\right]\sin(\Omega t)\} + (2\Omega \text{ terms}). \end{aligned} \tag{28}$$

When the photo diode signal is mixed with the phase-shifted modulation signal and low-pass filtered, the amplitude of the oscillating term with frequency Ω is preserved. When Ω is small compared to the cavity linewidth, the side bands are also in resonance with the cavity. The quantity $F(\omega)F^*(\omega+\Omega) - F^*(\omega)F(\omega-\Omega)$ is real, and by a simple Taylor expansion,

$$\begin{aligned} &F(\omega)F^*(\omega+\Omega) - F^*(\omega)F(\omega-\Omega) \\ \approx&\Omega F(\omega)\frac{d}{d\omega}F^*(\omega) + \Omega F^*(\omega)\frac{d}{d\omega}F(\omega) = \Omega\frac{d|F|^2}{d\omega}. \end{aligned} \tag{29}$$

Thus we can see that, with a small modulation frequency compared to the cavity linewidth, the derivative of the reflected power is measured. This dispersion curve is almost linear near the zero crossing and is the error signal used to generate feedback to the laser controller.

Our setup shown in Fig. 17 (a) differs from the one described above. Instead of phase modulation with an electro-optical modulator (EOM), we directly modulate the laser current to produce the sidebands. Also, we measure the cavity transmission rather than the reflection. This technique is investigated by Chow et al. [45]. They showed that when the modulation frequency is small compared to the cavity linewidth, the error signal is also proportional to the derivative of the transmission. The noise spectra of the locked laser for phase-modulation and

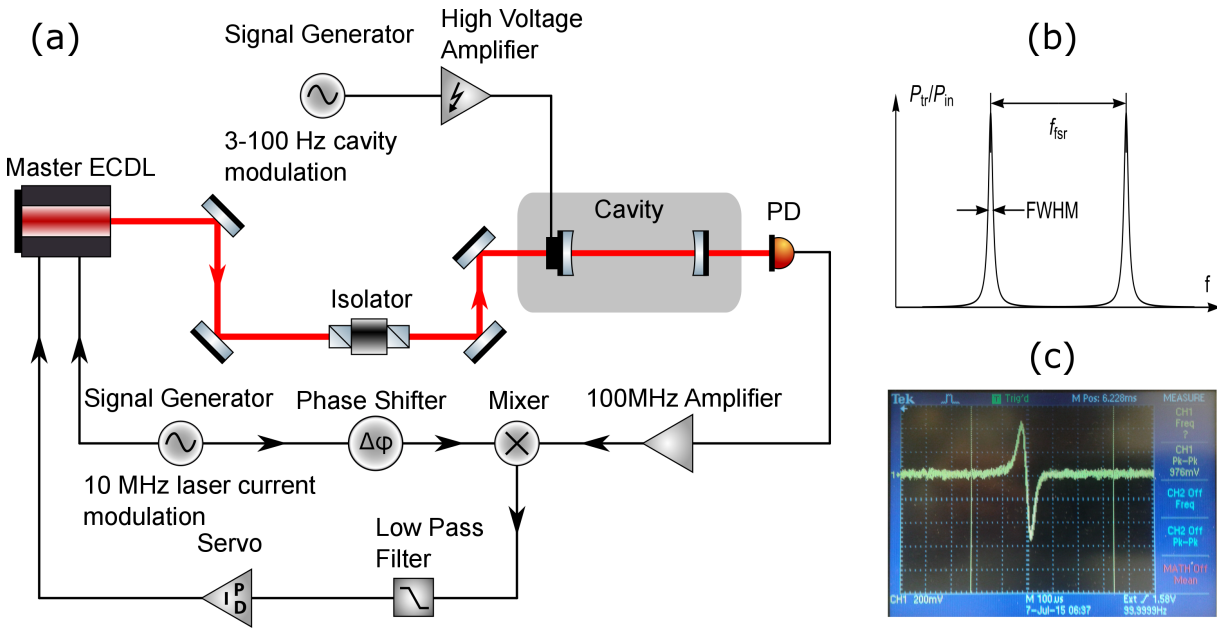

Figure 17: **a**. Pound-Drever-Hall locking setup. **b**. The transmission function of a FP cavity. **c**. The measured error signal after the low pass filter.

current-modulation are found to be nearly identical. However, a drawback of this setup is that the sidebands are present at every stage of the laser system.

In our setup, we have a 5.5 cm confocal cavity. The corresponding FSR is 1.4 GHz. The estimated cavity finesse is 100, giving a cavity linewidth of 14 MHz. We modulate the laser current at 10 MHz, so we expect to measure the derivative of the cavity transmission. The cavity length is scanned by a piezoelectric transducer with a frequency $f < 100$ Hz. This is equivalent with a scan in frequency space, because the changing cavity length changes the transmitted frequency. The measured error signal is shown in 17 (c), which confirms our expectation. We use a home-made servo circuit that contains a standard proportional-integral feedback loop. The servo bandwidth is set at 20 kHz, based on spectral noise measurement. The feedback is applied to both the piezo on the ECDL grating and the laser current. We use the root-mean-squared (RMS) voltage of the error signal at the zero crossing to estimate the laser linewidth

$$\Delta f = \frac{V_{\text{rms}}(V)}{\text{Error signal slope (V/Hz)}}. \tag{30}$$

The free-running linewidth is 3.5 MHz, while the locked linewidth is 140 kHz, which is less than 754 kHz, the transition linewidth. This should be sufficient for the experiment.

4 Iodine reference cell and saturated absorption spectroscopy

The master laser is locked to a stable FP-cavity to reduce its linewidth, and the cavity is locked to an iodine transition to cancel any slow drift of the cavity length. The transition wavenumber is at 15462.6 cm^{-1}, close to the half frequency of the ^{7}Li 2s-3p transition of 30925 cm^{-1}. The iodine lines close to this transition are shown in Fig. 18.

4.1 Principle of saturated absorption spectroscopy

Here we introduce the operating principle of saturated absorption spectroscopy [46]. Doppler broadening of a transition is due to the Doppler frequency shift of the laser light observed by moving atoms. The Doppler width for an atomic transition at room temperature is usually much larger compare to the natural transition linewidth. To obtain a Doppler-free measurement of the transition, the saturation absorption technique uses two overlapping laser beams, a low-intensity probe beam and a high intensity pump beam, that pass through the gas in opposite directions. The two beams have opposite Doppler shift, so they reacts with atoms with different velocities. However, when the laser frequency is on resonance, they both affect the atoms that are stationary in the beam direction. The pump beam pumps the atoms to an excited state, reducing the number of atoms that can absorb the probe beam. The probe beam intensity after the gas is measured, and a dip whose width is close to the natural linewidth should appear at the center of the Doppler broadened feature.

To keep it simple, we limit the discussion to a two level system. Let ω denote the laser angular frequency. The absorption coefficient for a laser beam with frequency ω is given by

$$\kappa(\omega) = \int N\Big(n_g(v) - n_e(v)\Big)\sigma(\omega - kv)dv, \tag{31}$$

in which N is the atom number, $n_g(v)$ and $n_e(v)$ are the probabilities of the atoms with speed v in the ground state and the excited states, respectively, and σ is the frequency dependent absorption cross-section. When the laser intensity is small, all the atoms are in the ground state, thus the total number density $n_g(v) = n(v)$ and $n_e(v) = 0$. The speed of the atoms in the beam direction obeys the Maxwell-Boltzmann distribution

$$n(v) = \frac{1}{\sqrt{\pi}u}\exp\left(-\frac{v^2}{u^2}\right), \tag{32}$$

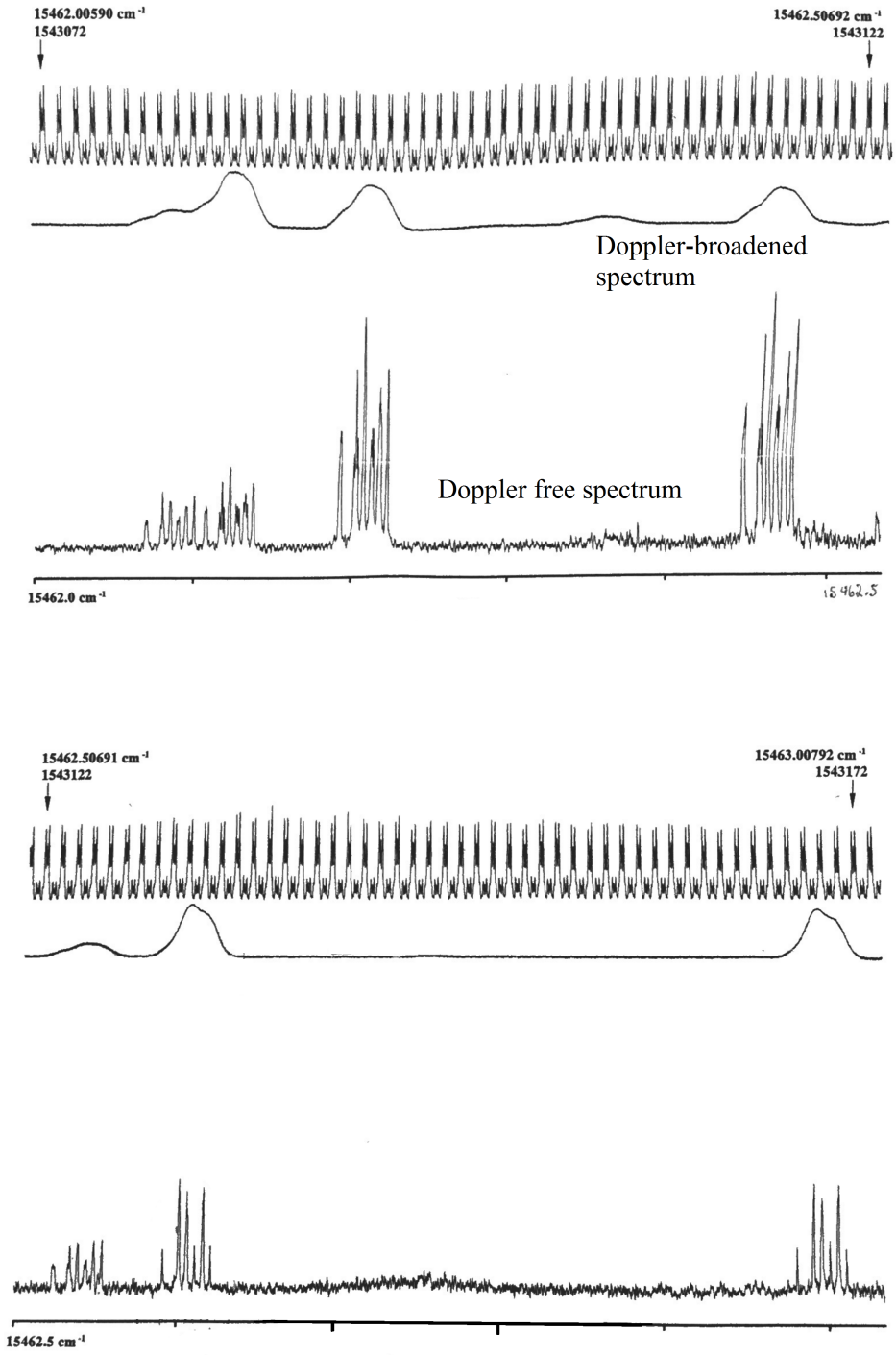

Figure 18: Atlas of the transitions for iodine at 15462 cm^{-1}. The feature at 15462.6 cm^{-1} will be used to lock the laser; however, during the testing process we use the larger feature at 15462.45 cm^{-1}.

in which $u = \sqrt{2\pi k_B T/m}$. The cross section is proportional to a Lorentzian line shape function, i.e. $\sigma(\omega) = \frac{g_2}{g1}\frac{\pi^2 c^2}{\omega_0^2} g_H(\omega)$,

$$g_H(\omega) = \frac{1}{2\pi}\frac{\Gamma}{(\omega-\omega_0)^2 + \Gamma^2/4}, \tag{33}$$

in which ω_0 is the resonance frequency in the lab frame, and Γ is the natural linewidth of the transition. To calculate the Doppler broadened line shape function, $g_D(\omega)$, we take Eq. (32) and Eq. (33) into Eq. (31),

$$g_D(\omega) \propto \int_{-\infty}^{\infty} g_H(\omega - kv) n(v) dv \tag{34}$$

Because the Lorentzian $g_H(\omega - kv)$ is only nonzero for a small region of v, it can be regarded as the delta function. We require that $\int g_D(\omega) d\omega = 1$, thus we have

$$g_D(\omega) = \frac{c}{u\omega_0\sqrt{\pi}} \exp\left(-\frac{c^2}{u^2}\left(\frac{\omega-\omega_0}{\omega_0}\right)^2\right). \tag{35}$$

The FWHM of this Gaussian line shape is $\Delta\omega_D = 2\sqrt{\ln(2)}\frac{u}{c}\omega_0$. As an example, for ^{7}Li $2\,^2S_{1/2}$ to $2\,^2P_{3/2}$ transition at 671 nm, this width is 2.1 GHz, whereas the natural transition linewidth is 5.9 MHz.

Now we consider the case when the laser intensity is large. Here n_e is no longer zero. From the optical Bloch equations we can derive the steady state probabilities satisfy the following relation

$$n_g - n_e = \frac{1}{1 + 2I/I_s}, \tag{36}$$

in which I_s is the saturation intensity. If we take this back into Eq. (31), and follow that same argument from above, we find that the absorption coefficient at a high intensity decreases from the zero-intensity limit by a factor of $1/(1 + 2I/I_s)$. Thus, as the laser intensity increases, the peak absorption of the Doppler broadened spectrum should decrease.

Now we split the laser beam into a low intensity probe beam and a high intensity pump beam, and pass them through the atom gas in opposite directions. The probe transmission is shown in Fig. 19 (a). We need to consider two cases, shown in Fig. 19 (b) and (c). First, if the laser is off resonance, i.e. $\omega \neq \omega_0$, then the resonance condition $\omega - kv = \omega_0$ is different for the pump and the probe. For the probe, we still have $n_e = 0$, thus the absorption is the same with and without the pump. Second, if the laser is on resonance, then both the beams react with the atoms that are stationary in the beam direction ($v = 0$). For the probe, the ground and excited

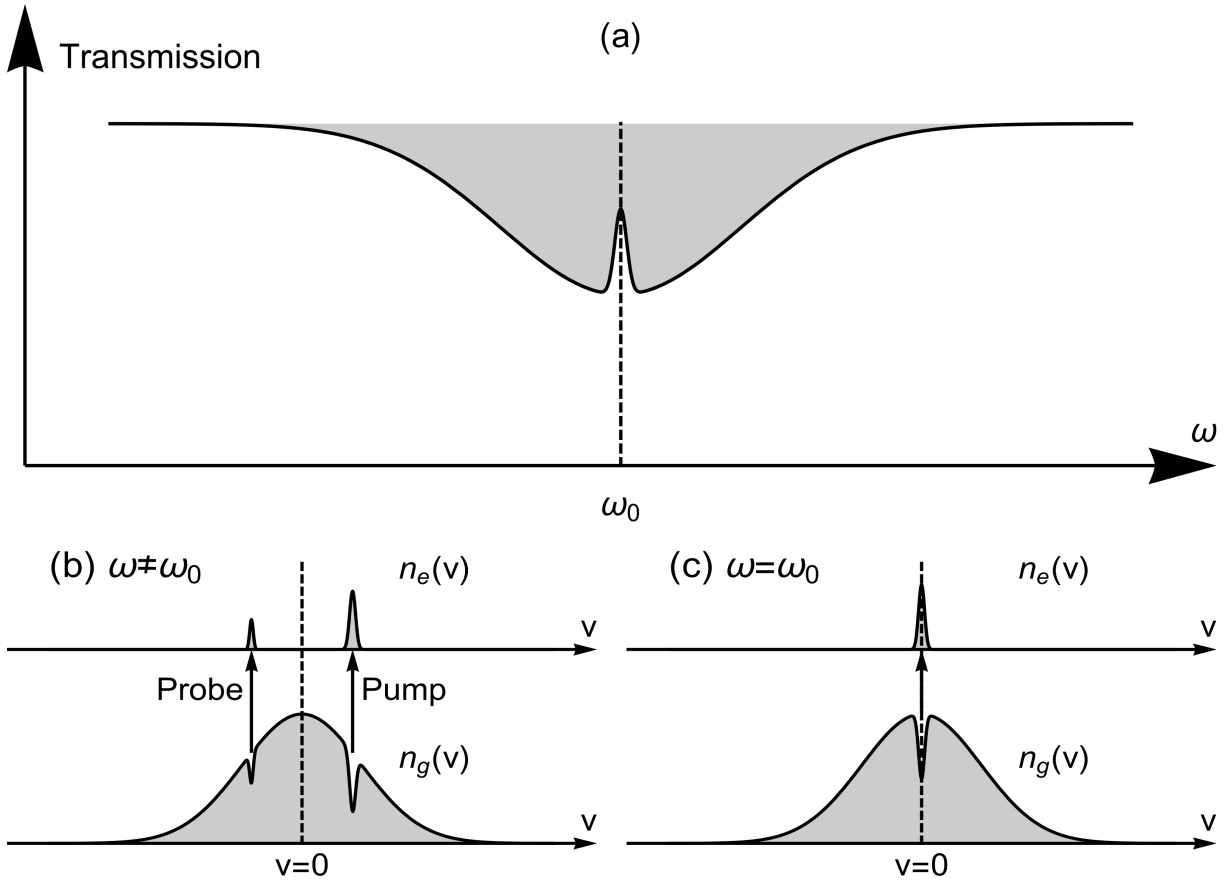

Figure 19: **a**. Transmission of the probe beam. The presence of a high power pump beam reduces the probe beam absorption at ω_0. **b**. Ground and excited state number density versus particle speed, v, in the beam direction. When the laser frequency is off resonance, the pump and the probe are absorbed by atoms with different speed. **c**. When the laser frequency is on resonance, the pump and the probe reacts to atoms that are stationary in the beam direction. The pump beam creates population inversion, so that fewer atom can absorb the probe beam.

probabilities are $ng = n_e = 1/2$, if the pump intensity $I_{pump} \gg I_{sat}$, thus no atoms in the ground state can absorb any probe light. The "hole" burnt in the absorption profile has a width that is equal to the powered broadened width of the transition, i.e. $\Delta\omega = \Gamma(1 + I/I_s)^{1/2}$.

4.2 Experiment

The experimental schematic is shown in Fig. 20. The output of the slave laser goes through a pair of lenses ($f = 150$ mm) to ensure that the beam size is nearly constant within the cell. A half-waveplate and PBS combination is used to continuously vary the power ratio between the pump and probe beams. Because the windows of the cell are at Brewster's angle, an additional half-waveplate is used to change the probe beam from s-polarized to p-polarized to minimize reflection loss. The beam is triple-passed through the cell using a pair of D-shaped

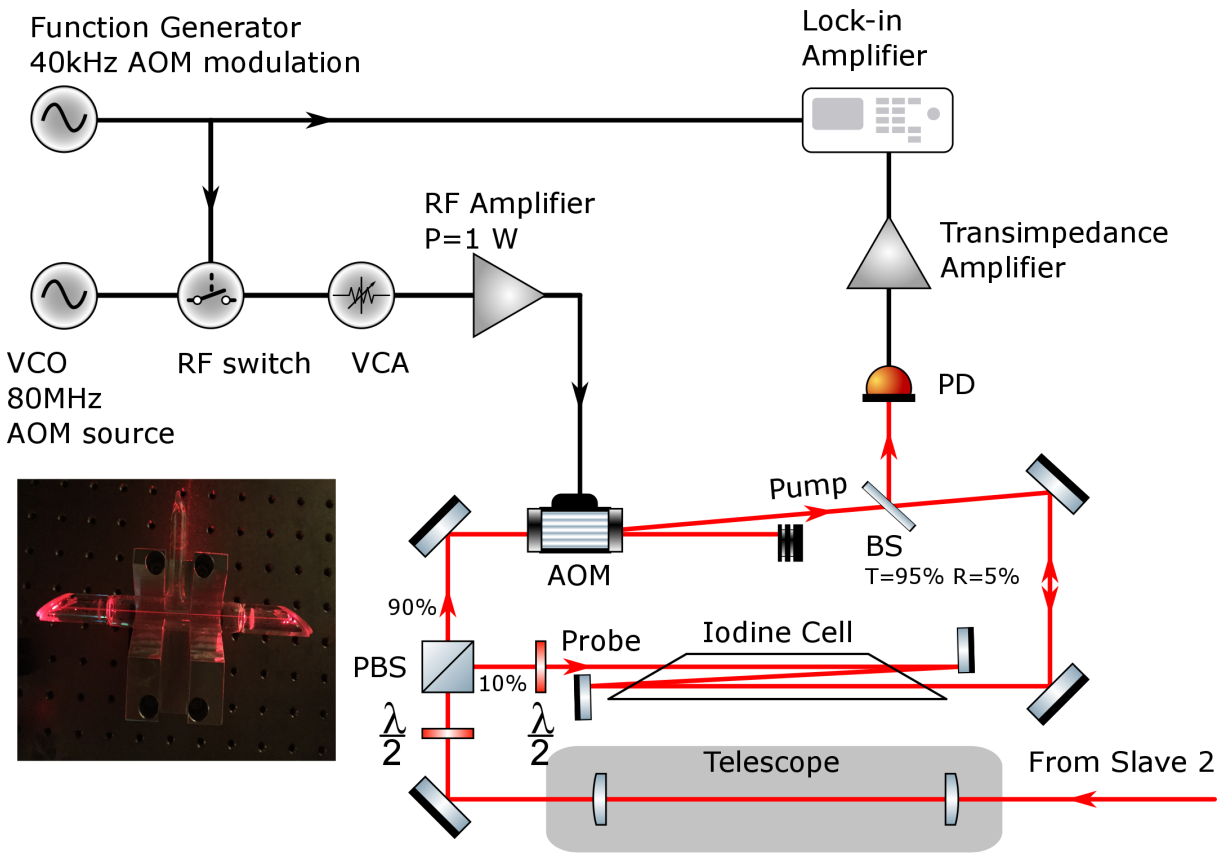

Figure 20: Schematics for the Iodine cell saturation spectroscopy. VCO: voltage-controlled oscillator. VCA: voltage-controlled attenuator. Inset: fluorescence of the Iodine cell at 15462.45 cm^{-1}.

mirrors, increasing the interaction length. The transmitted probe beam is measured using a fast photo-diode. The pump beam goes through an acousto-optical modulator (AOM) for intensity modulation. The first-order beam is overlapped with the probe and passes through the cell in the opposite direction.

First we measured the Doppler broadened feature at 15462.45 cm^{-1}. The master laser is tuned to the frequency and locked to the FP cavity. To scan the laser frequency, the cavity length is modulated with a triangular wave at 3 Hz. We verify that both slave lasers remain injection-locked for about 3 GHz of scanning, with 20 mW in the probe beam. The transmission through the cell is measured. In order to normalize the signal, we take out the cell, and measure the probe power variation during the frequency scan. The normalized transmission signal is shown in Fig. 21 (a). The maximum absorption is 8%, and the FWHM is 1 GHz, which is consistent with the same feature shown in the atlas. Staying at the center frequency, we vary the probe power from 0 to 40 mW and measure the peak absorption as a function of the beam intensity.

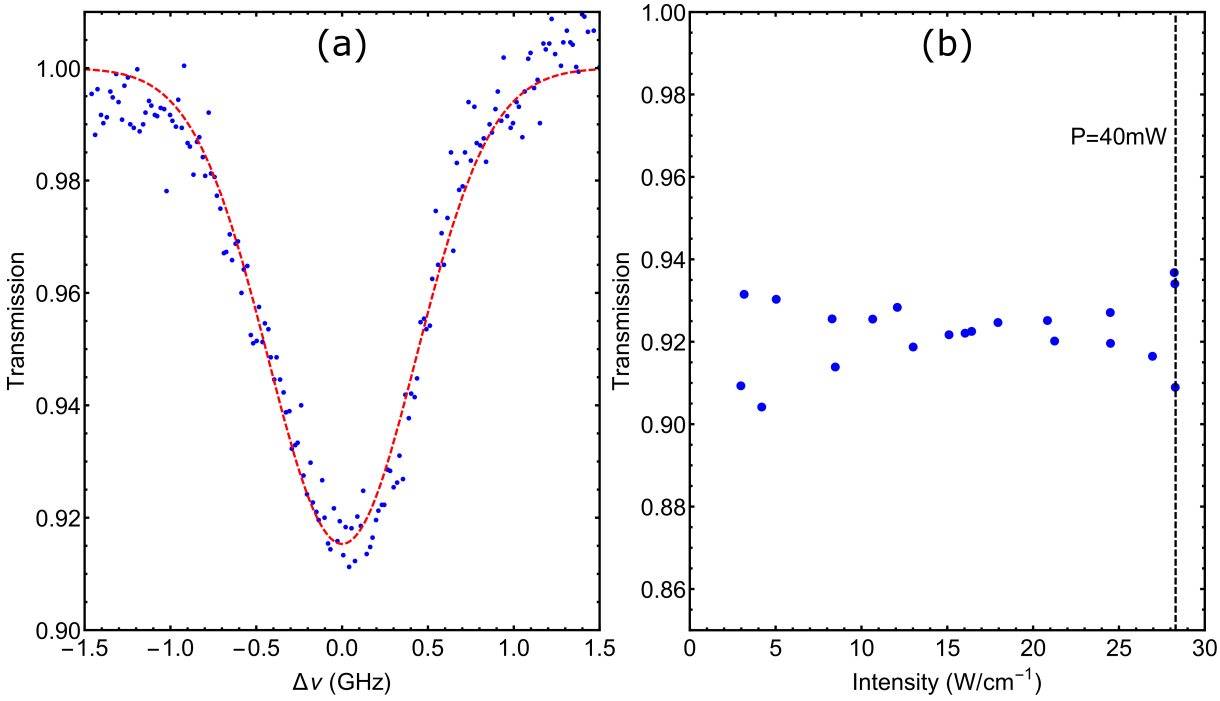

Figure 21: Measurement of the Doppler broadened Iodine feature. a. The Doppler broadened signal at 15462.45 cm^{-1}. The peak absorption is at 8%. **b**. Peak absorption measured as a function of beam intensity. The intensity is changed by varying the optical power. The peak absorption is constant over the measured range, indicating that the saturation intensity is much higher than the level we can reach.

The result is shown in Fig. 21 (b). We can see that even at 28 W/cm^2, there is no sign of saturation for the transition. Therefore the intensity we have is only a small fraction of I_{sat}. We cannot increase the beam intensity by reducing the beam waist, because if we did, the Rayleigh range would be reduced, and the beam intensity would no longer be constant throughout the cell. Increasing the beam power is also not an option, because the slave laser is already running at its maximum current. As a consequence, the signal to noise ratio of the Doppler-free features will be small and requires a lock-in detection technique to be observed. Therefore, we need to modulate the pump beam and use a lock-in amplifier to detect the Doppler-free lines.

A lock-in amplifier can detect signals with a reference frequency from a noisy environment. A schematic of the device is shown in Fig. 22. If we denote the input and the reference signal after the phase shifter as

$$V_{\text{in}} = V_0 \cos(\omega_{\text{ref}} t) + V_{\text{noise}} \tag{37}$$

$$V_{\text{ref}} = V_1 \cos(\omega_{\text{ref}} t + \varphi), \tag{38}$$

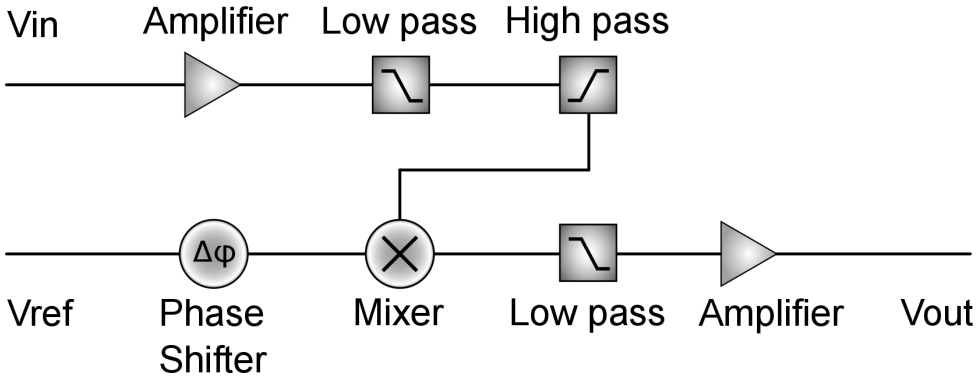

Figure 22: Schematic of the lock-in amplifier.

then the output signal of the mixer is

$$V_{mix} = \frac{1}{2} V_0 V_1 \left(\cos\varphi + \cos\left(2\omega_{\text{ref}} t + \varphi\right)\right). \tag{39}$$

After the low pass filter, the original signal V_0 is recovered, whereas the noise is rejected by the bandpass filters on the input side and the low-pass filter on the output side. In order to optimize the detected signals, the phase shift, the band-pass and low-pass filter frequencies need to be fine-tuned.

A high modulation frequency can isolate the extracted signal from environmental noise. Therefore, instead of mechanical shutters, we use an AOM for intensity modulation. A voltage controlled oscillator (VCO) is used to generate the (40 kHz) modulation frequency, and the signal is applied to the RF switch. The modulation signal is also used as the reference to the lock-in amplifier. The voltage controlled attenuator (VCA) is set to a fixed voltage to maintain the maximum RF amplifier output power (1 W). The AOM is operating at 80 MHz, resulting in a frequency shift of the pump relative to probe. This will cause the beams to interact with atoms with a small velocity along the beam direction. However, as long as the frequency shift is small compared to the Doppler width, the conclusions of the Doppler free spectrum still apply. The AOM we use is rated for 3 W power, but the input power is 1 W, limited by the amplifier. The AOM efficiency is 45%; however, this is sufficient for our purpose.

With this configuration we measure the Doppler-free lines at 15462.45 cm^{-1}, which is shown in Fig. 23. The horizontal axis is the FP cavity scanning voltage, which is inversely related to the laser frequency. The vertical axis is the lock-in amplifier output. We find that the laser can only scan 1.5 GHz, because the slave lasers are operating at full power. Outside of

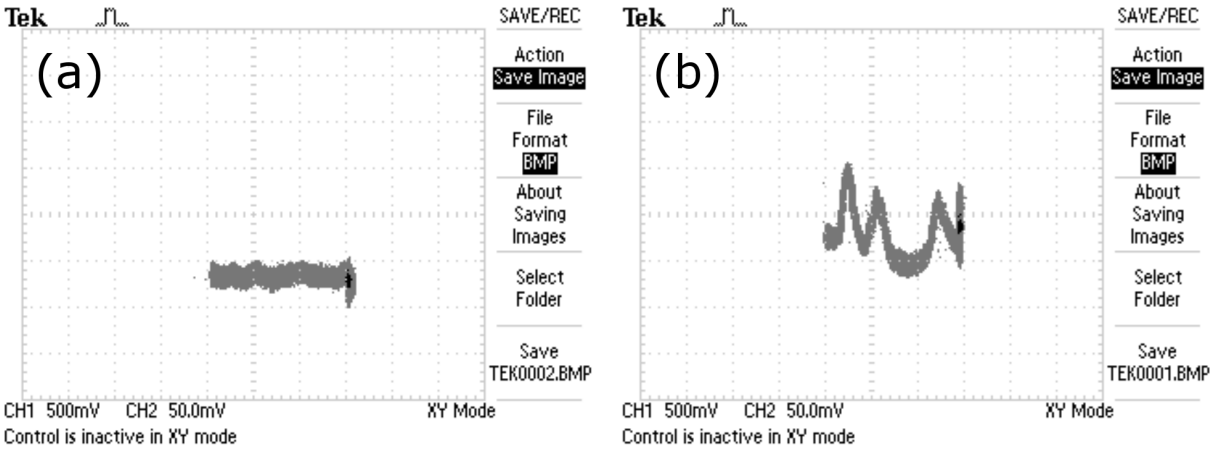

Figure 23: Lock-in amplifier output signal as a function of the cavity scanning voltage, with the pump beam blocked in (a) and unblocked in (b). The frequency of the master laser is centered at 15462.45 cm^{-1}, and the scanning range is 1.5 GHz. Higher cavity scan voltage corresponds to lower frequency.

this range they do not remain injection-locked. Three peaks were recorded, and measurement is performed with the pump beam blocked to verify that the peaks are not just noise. The signals that we observed are not optimized yet, because the slave lasers are unstable during the frequency scan. To improve the signal to noise ratio, we plan to reduce the scanning frequency of the laser to well below 1 Hz, to optimize the alignment for injection, and to fine tune the lock-in amplifier settings.

Once we obtain the Doppler-free spectrum, we can add another mixer to mix the amplified PD signal and the 10 MHz laser modulation. The product is used as the lock-in amplifier input, using the PDH technique to obtain an error signal that has a zero-crossing.

5 Conclusion and future work

In order to construct a UV MOT for narrow line cooling of ^{7}Li, we designed and built a frequency-doubling cavity with a BBO crystal to convert laser light at 646 nm to 323 nm. A master ECDL is used to generate 646 nm light and to inject a slave laser, which is used to seed the TA. The TA produces 250 mW light to be mode-matched into the doubling cavity. Alternatively, a fiber laser SFG approach with a PPLN crystal is potentially capable of generating a much higher power of about 2 W at 646 nm.

To ensure the frequency stability of the laser system, we have implemented a two stage locking scheme for the master laser frequency. The first stage is locking to a FP-cavity using a Pound-Drever-Hall technique. The linewidth of the locked laser is 140 kHz, while the free-running linewidth is 3.5 MHz. The second stage is locking to an iodine transition near 646.6 nm, via saturation absorption spectroscopy. Since the Doppler-free signal has a small amplitude, a lock-in amplifier is used to detect the frequency modulated absorption signal.

Currently, we need to complete the doubling cavity alignment, and optimize the SHG power. Additionally, a feedback circuit is needed to stabilize the doubling cavity. We also need to optimize the Doppler free signal of the iodine transition, and build the feedback electronics for the laser lock.

Once these procedures are completed, we need to use the UV beam to build a UV MOT. This requires that we split the UV into six beams that have equal intensity at the center of the experiment chamber. Additionally, the size of the beams need to match the size of the red MOT. Furthermore, we will use AOMs to adjust the frequency detuning, in order to optimize the cooling efficiency.

References

[1] K. E. Strecker, G. B. Partridge, A. G. Truscott, and R. G. Hulet, "Formation and propagation of matter-wave soliton trains", Nature 417, 150153 (2002).

[2] B. A. Malomed, "Soliton Management in Periodic Systems", Springer, 2005.

[3] E. Braaten, H. W. Hammer, "Efimov physics in cold atoms", Annals of Physics, Volume 322, Issue 1, 120163, 2007.

[4] M. R. Matthews, B. P. Anderson, P. C. Haljan, D. S. Hall, C. E. Wieman, and E. A. Cornell, "Vortices in a Bose-Einstein Condensate", Phys. Rev. Lett. 83, 2498 (1999).

[5] M. H. Anderson, J. R. Ensher, M. R. Matthews, C. E. Wieman, E.A. Cornell,"Observation of Bose Einstein Condensation in a Dilute Atomic Vapor", Science 269, 5221, 198, (1995).

[6] C. C. Bradley, C. A. Sackett, J. J. Tollett, and R. G. Hulet, "Evidence of Bose Einstein Condensation in an Atomic Gas with Attractive Interactions," Phys. Rev. Lett. 75, 16871690 (1995)

[7] K. B. Davis, M. O. Mewes, M. R. Andrews, N. J. van Druten, D. S. Durfee, D. M. Kurn, and W. Ketterle, "Bose-Einstein Condensation in a Gas of Sodium Atoms", Phys. Rev. Lett. 75, 3969 (1995).

[8] H. J. Metcalf, P. van der Straten, "Laser Cooling and Trapping", Springer, 2009.

[9] W. D. Phillips and H. Metcalf, "Laser Deceleration of an Atomic Beam", Phys. Rev. Lett. 48, 596 (1982).

[10] D. E. Pritchard, "Cooling Neutral Atoms in a Magnetic Trap for Precision Spectroscopy", Phys. Rev. Lett. 51, 1336 (1983).

[11] R. Grimm, M. Weidemuller, Y. B. Ovchinnikov, "Optical Dipole Traps for Neutral Atoms", Advances In Atomic, Molecular, and Optical Physics, Volume 42, 2000, Pages 95170.

[12] D. F. Dries, "Transport Properties of a Bose-Einstein Condensate with Tunable Interactions in the Presence of a Disordered or Single Defect Potential", Ph.D. Thesis, Rice University (2010).

[13] J. Dalibard and C. Cohen-Tannoudji, "Laser cooling below the Doppler limit by polarization gradients: simple theoretical models", Journal of the Optical Society of America B Vol. 6, Issue 11, pp. 2023-2045 (1989).

[14] D. S. Weiss, E. Riis, Y. Shevy, P. J. Ungar, and Steven Chu, "Optical molasses and multilevel atoms: experiment", Journal of the Optical Society of America B Vol. 6, Issue 11, pp. 2072-2083 (1989).

[15] P. Hamilton, G. Kim, T. Joshi, B. Mukherjee, D. Tiarks, and H. Muller, "Sisyphus cooling of lithium", Phys. Rev. A 89, 023409, (2014).

[16] A. T. Grier, I. Ferrier-Barbut, B. S. Rem, M. Delehaye, L. Khaykovich, F. Chevy, and C. Salomon, "Λ-enhanced sub-Doppler cooling of lithium atoms in D1 gray molasses", Phys. Rev. A. 87, 063411 (2013).

[17] S. J. M. Kuppens, K. L. Corwin, K. W. Miller, T. E. Chupp, and C. E. Wieman, "Loading an optical dipole trap", Phys. Rev. A, 62, 013406 (2000).

[18] Ralchenko et. al. "Nist atomic spectra database", http://physics.nist.gov/asd3, 2010.

[19] W. R. Johnson, U. I. Safronova, A. Derevianko, M. S. Safronova, "Relativistic many-body calculation of energies, lifetimes, hyperfine constants, and polarizabilities in ^{7}Li", Phys. Rev. A. 77, 022510 (2008).

[20] W. I. McAlexander, E. R. I. Abraham, and R. G. Hulet, "Radiative lifetime of the 2P state of lithium", Phys. Rev. A 54, R5(R), (1996).

[21] P. M. Duarte, R. A. Hart, J. M. Hitchcock, T. A. Corcovilos, T. L. Yang, A. Reed, and R. G. Hulet, "All-optical production of a lithium quantum gas using narrow-line laser cooling", Phys Rev A 84, 061406(R) (2011).

[22] M. S. Safronova, U. I. Safronova, and C. W. Clark, "Magic wavelengths for optical cooling and trapping of lithium", Phys. Rev. A 86, 042505 (2012).

[23] The commercial frequency doubler used in APP3 is TA/DL-SHG 110 from Toptica Photonics.

[24] A. C. Wilson, C. Ospelkaus, A. P. VanDevender, J. A. Mlynek, K. R. Brown, D. Leibfried, and D.J.Wineland, "A 750-mW, continuous-wave, solid-state laser source at 313 nm for cooling and manipulating trapped $^{9}Be^{+}$ ions", Appl. Phys. B, 105:741748, (2011).

[25] A. Omran, "A Microscope for Fermi Gases", Ph.D thesis, Ludwig Maximilian University of Munich, 2016.

[26] W. P. Risk, T. R. Gosnell, and A. V. Nurmikko, "Compact Blue-Green Lasers", Cambridge University Press, 2003.

[27] T. Y. Fan, C. E. Huang, B. Q. Hu, R. C. Eckardt, Y. X. Fan, R. L. Byer, and R. S. Feigelson, "Second harmonic generation and accurate index of refraction measurements in flux-grown $KTiOPO_4$", Applied Optics, 26, 12, (1987).

[28] G. D. Boyd and D. A. Kleinman, "Parametric Interaction of Focused Gaussian Light Beams", Journal of Applied Physics 39, 3597 (1968).

[29] Y. F. Chen and Y. C. Chen, "Analytical functions for the optimization of second-harmonic generation and parametric generation by focused Gaussian beams", Appl. Phys. B 76, 645647 (2003).

[30] A. V. Smith, http://www.as-photonics.com/snlo.

[31] T. Freegarde, J. Coutts, J. Walz, D. Leibfried, and T. W. Hansch, "General analysis of type I second-harmonic generation with elliptical Gaussian beams", Journal of the Optical Society of America B Vol. 14, Issue 8, pp. 2010-2016 (1997).

[32] T. Freegarde, C. Zimmermann, "On the design of enhancement cavities for second-harmonic generation", Optics Communications 199, 435 (2001).

[33] A. Dienes, H. Kogelnik, E. Ippen and C. Shank, “Astigmatically compensated cavities for CW dye lasers”, IEEE Journal of Quantum Electronics QE-8, 373 (1972).

[34] K. R. Lykke, “Internally-coupled build-up cavity for frequency doubling of cw lasers”, Optics Communications 157, 8892, (1998).

[35] Z. Y. Ou, S. E Pereira, E. S. Polzik, and H. J. Kimble, “85% efficiency for cw frequency doubling from 1.08 to 0.54 um”, Optics Letters, Vol. 17, No. 9, (1992).

[36] G. C. Bhar, U. Chatterjee, and S. Das, “Tunable near-infrared radiation by difference frequency mixing in beta barium borate crystal”, Applied Physics Letters 58.3, 231-233, (1991).

[37] A. E. Siegman, “Lasers”, University Science Books, (1986).

[38] C. J. Hawthorn, K. P. Weber and R. E. Scholten, “Littrow configuration tunable external cavity diode laser with fixed direction output beam”, Rev. Sci. Instrum. 72, 4477 (2001).

[39] J. C. B. Kangara et al. “Design and construction of cost-effective tapered amplifier systems for laser cooling and trapping experiments”, Am. J. Phys. 82, 805 (2014).

[40] Eugene Hecht, “Optics”, Addison-Wesley Publishing Company, London, (1974).

[41] M. Yamada, N. Nada, M. Saitoh, and K. Watanabe, “First-order quasi-phase matched LiNbO3 waveguide periodically poled by applying an external field for efficient blue second-harmonic generation”, Applied Physics Letters, 62, 5, (1993).

[42] E. S. Polzik and H. J. Kimble, “Frequency doubling with KNbO3 in an external cavity”, Optics Letters 16, 18, (1991).

[43] R. W. P. Drever, J. L. Hall, F. V. Kowalski, J. Hough, G. M. Ford, A. J. Munley, H. Ward, “Laser phase and frequency stabilization using an optical resonator”, Appl. Phys. B. 31, 2, 97-105, (1983).

[44] E. D. Black, “An Introduction to Pound-Drever-Hall laser frequency stabilization”, Am. J. Phys. 69, 79 (2001).

[45] J. H. Chow, J. S. Cumpston, I. C. M. Littler, D. E. McClelland, and M. B. Gray, “Interrogation of a fiber Fabry-Perot sensor by current modulation of a diode laser”, Lasers and Electro-Optics Society, 2005.

[46] C. J. Foot, “Atomic Physics”, Oxford University Press, 2005.

[47] D. W. Preston, “Doppler-free saturated absorption: Laser spectroscopy”, American Journal of Physics. 64 (11), 1432 (1996).